Radio measurements of the depth of air-shower maximum at the Pierre Auger Observatory

(Article begins on next page)

26 December 2024

Radio Measurements of the Depth of Air-Shower Maximum at the Pierre Auger Observatory

A. Abdul Halim[13], P. Abreu[73], M. Aglietta[55,53], I. Allekotte[1], K. Almeida Cheminant[71], A. Almela[7,12], R. Aloisio[46,47], J. Alvarez-Muñiz[79], J. Ammerman Yebra[79], G.A. Anastasi[55,53], L. Anchordoqui[86], B. Andrada[7], S. Andringa[73], Anukriti[76], L. Apollonio[60,50], C. Aramo[51], P.R. Araújo Ferreira[43], E. Arnone[64,53], J.C. Arteaga Velázquez[68], P. Assis[73], G. Avila[11], E. Avocone[58,47], A. Bakalova[33], F. Barbato[46,47], A. Bartz Mocellin[85], J.A. Bellido[13,70], C. Berat[37], M.E. Bertaina[64,53], G. Bhatta[71], M. Bianciotto[64,53], P.L. Biermann[i], V. Binet[5], K. Bismark[40,7], T. Bister[80,81], J. Biteau[38,b], J. Blazek[33], C. Bleve[37], J. Blümer[42], M. Boháčová[33], D. Boncioli[58,47], C. Bonifazi[8,27], L. Bonneau Arbeletche[22], N. Borodai[71], J. Brack[k], P.G. Brichetto Orchera[7], F.L. Briechle[43], A. Bueno[78], S. Buitink[15], M. Buscemi[48,62], M. Büsken[40,7], A. Bwembya[80,81], K.S. Caballero-Mora[67], S. Cabana-Freire[79], L. Caccianiga[60,50], R. Caruso[59,48], A. Castellina[55,53], F. Catalani[19], G. Cataldi[49], L. Cazon[79], M. Cerda[10], A. Cermenati[46,47], J.A. Chinellato[22], J. Chudoba[33], L. Chytka[34], R.W. Clay[13], A.C. Cobos Cerutti[6], R. Colalillo[61,51], A. Coleman[90], M.R. Coluccia[49], R. Conceição[73], A. Condorelli[38], G. Consolati[50,56], M. Conte[57,49], F. Convenga[58,47], D. Correia dos Santos[29], P.J. Costa[73], C.E. Covault[84], M. Cristinziani[45], C.S. Cruz Sanchez[3], S. Dasso[4,2], K. Daumiller[42], B.R. Dawson[13], R.M. de Almeida[29], J. de Jesús[7,42], S.J. de Jong[80,81], J.R.T. de Mello Neto[27,28], I. De Mitri[46,47], J. de Oliveira[18], D. de Oliveira Franco[22], F. de Palma[57,49], V. de Souza[20], B.P. de Souza de Errico[27], E. De Vito[57,49], A. Del Popolo[59,48], O. Deligny[35], N. Denner[33], L. Deval[42,7], A. di Matteo[53], M. Dobre[74], C. Dobrigkeit[22], J.C. D'Olivo[69], L.M. Domingues Mendes[73], Q. Dorosti[45], J.C. dos Anjos[16], R.C. dos Anjos[26], J. Ebr[33], F. Ellwanger[42], M. Emam[80,81], R. Engel[40,42], I. Epicoco[57,49], M. Erdmann[43], A. Etchegoyen[7,12], C. Evoli[46,47], H. Falcke[80,82,81], J. Farmer[89], G. Farrar[88], A.C. Fauth[22], N. Fazzini[f], F. Feldbusch[41], F. Fenu[42,e], A. Fernandes[73], B. Fick[87], J.M. Figueira[7], A. Filipčič[77,76], T. Fitoussi[42], B. Flaggs[90], T. Fodran[80], T. Fujii[89,g], A. Fuster[7,12], C. Galea[80], C. Galelli[60,50], B. García[6], C. Gaudu[39], H. Gemmeke[41], F. Gesualdi[7,42], A. Gherghel-Lascu[74], P.L. Ghia[35], U. Giaccari[49], J. Glombitza[43,h], F. Gobbi[10], F. Gollan[7], G. Golup[1], M. Gómez Berisso[1], P.F. Gómez Vitale[11], J.P. Gongora[11], J.M. González[1], N. González[7], I. Goos[1], D. Góra[71], A. Gorgi[55,53], M. Gottowik[79], T.D. Grubb[13], F. Guarino[61,51], G.P. Guedes[23], E. Guido[45], L. Gülzow[42], S. Hahn[40], P. Hamal[33], M.R. Hampel[7], P. Hansen[3], D. Harari[1], V.M. Harvey[13], A. Haungs[42], T. Hebbeker[43], C. Hojvat[f], J.R. Hörandel[80,81], P. Horvath[34], M. Hrabovský[34], T. Huege[42,15], A. Insolia[59,48], P.G. Isar[75], P. Janecek[33], V. Jilek[33], J.A. Johnsen[85], J. Jurysek[33], K.-H. Kampert[39], B. Keilhauer[42], A. Khakurdikar[80], V.V. Kizakke Covilakam[7,42], H.O. Klages[42], M. Kleifges[41], F. Knapp[40], J. Köhler[42], N. Kunka[41], B.L. Lago[17], N. Langner[43], M.A. Leigui de Oliveira[25], Y. Lema-Capeans[79], A. Letessier-Selvon[36], I. Lhenry-Yvon[35], L. Lopes[73], L. Lu[91], Q. Luce[40], J.P. Lundquist[76], A. Machado Payeras[22], M. Majercakova[33], D. Mandat[33], B.C. Manning[13], P. Mantsch[f], S. Marafico[35], F.M. Mariani[60,50], A.G. Mariazzi[3], I.C. Mariş[14], G. Marsella[62,48], D. Martello[57,49], S. Martinelli[42,7], O. Martínez Bravo[65], M.A. Martins[79], H.-J. Mathes[42], J. Matthews[a], G. Matthiae[63,52], E. Mayotte[85,39], S. Mayotte[85], P.O. Mazur[f], G. Medina-Tanco[69], J. Meinert[39], D. Melo[7], A. Menshikov[41], C. Merx[42], S. Michal[34], M.I. Micheletti[5], L. Miramonti[60,50], S. Mollerach[1], F. Montanet[37], L. Morejon[39], C. Morello[55,53], K. Mulrey[80,81], R. Mussa[53], W.M. Namasaka[39], S. Negi[33], L. Nellen[69], K. Nguyen[87], G. Nicora[9], M. Niechciol[45], D. Nitz[87], D. Nosek[32], V. Novotny[32], L. Nožka[34], A. Nucita[57,49], L.A. Núñez[31], C. Oliveira[20], M. Palatka[33], J. Pallotta[9], S. Panja[33], G. Parente[79], T. Paulsen[39], J. Pawlowsky[39], M. Pech[33], J. Pękala[71], R. Pelayo[66], L.A.S. Pereira[24], E.E. Pereira Martins[40,7], J. Perez Armand[21], C. Pérez Bertolli[7,42], L. Perrone[57,49], S. Petrera[46,47], C. Petrucci[58,47], T. Pierog[42], M. Pimenta[73], M. Platino[7], B. Pont[80], M. Pothast[81,80], M. Pourmohammad Shahvar[62,48], P. Privitera[89], M. Prouza[33], A. Puyleart[87], S. Querchfeld[39], J. Rautenberg[39], D. Ravignani[7], J.V. Reginatto Akim[22], M. Reininghaus[40], J. Ridky[33], F. Riehn[79], M. Risse[45], V. Rizi[58,47], W. Rodrigues de Carvalho[80], E. Rodriguez[7,42], J. Rodriguez Rojo[11], M.J. Roncoroni[7], S. Rossoni[44], M. Roth[42], E. Roulet[1], A.C. Rovero[4], P. Ruehl[45], A. Saftoiu[74], M. Saharan[80], F. Salamida[58,47], H. Salazar[65], G. Salina[52], J.D. Sanabria Gomez[31], F. Sánchez[7], E.M. Santos[21], E. Santos[33], F. Sarazin[85], R. Sarmento[73], R. Sato[11], P. Savina[91], C.M. Schäfer[40], V. Scherini[57,49], H. Schieler[42], M. Schimassek[35], M. Schimp[39], D. Schmidt[42], O. Scholten[15,j], H. Schoorlemmer[80,81], P. Schovánek[33], F.G. Schröder[90,42], J. Schulte[43], T. Schulz[42], S.J. Sciutto[3], M. Scornavacche[7,42], A. Segreto[54,48], S. Sehgal[39], S.U. Shivashankara[76], G. Sigl[44], G. Silli[7], O. Sima[74,c], K. Simkova[15], F. Simon[41], R. Smau[74], R. Šmída[89], P. Sommers[l], J.F. Soriano[86], R. Squartini[10], M. Stadelmaier[50,60,42], S. Stanič[76], J. Stasielak[71], P. Stassi[37], S. Strähnz[40], M. Straub[43], T. Suomijärvi[38], A.D. Supanitsky[7], Z. Svozilikova[33], Z. Szadkowski[72], F. Tairli[13], A. Tapia[30], C. Taricco[64,53], C. Timmermans[81,80], O. Tkachenko[42], P. Tobiska[33], C.J. Todero Peixoto[19], B. Tomé[73], Z. Torrès[37], A. Travaini[10], P. Travnicek[33], C. Trimarelli[58,47],

M. Tueros[3], M. Unger[42], L. Vaclavek[34], M. Vacula[34], J.F. Valdés Galicia[69], L. Valore[61,51], E. Varela[65],
A. Vásquez-Ramírez[31], D. Veberič[42], C. Ventura[28], I.D. Vergara Quispe[3], V. Verzi[52], J. Vicha[33], J. Vink[83],
S. Vorobiov[76], C. Watanabe[27], A.A. Watson[d], A. Weindl[42], L. Wiencke[85], H. Wilczyński[71], D. Wittkowski[39],
B. Wundheiler[7], B. Yue[39], A. Yushkov[33], O. Zapparrata[14], E. Zas[79], D. Zavrtanik[76,77], M. Zavrtanik[77,76]

(Pierre Auger Collaboration)

[1]: *Centro Atómico Bariloche and Instituto Balseiro (CNEA-UNCuyo-CONICET), San Carlos de Bariloche, Argentina*
[2]: *Departamento de Física and Departamento de Ciencias de la Atmósfera y los Océanos, FCEyN, Universidad de Buenos Aires and CONICET, Buenos Aires, Argentina*
[3]: *IFLP, Universidad Nacional de La Plata and CONICET, La Plata, Argentina*
[4]: *Instituto de Astronomía y Física del Espacio (IAFE, CONICET-UBA), Buenos Aires, Argentina*
[5]: *Instituto de Física de Rosario (IFIR) – CONICET/U.N.R. and Facultad de Ciencias Bioquímicas y Farmacéuticas U.N.R., Rosario, Argentina*
[6]: *Instituto de Tecnologías en Detección y Astropartículas (CNEA, CONICET, UNSAM), and Universidad Tecnológica Nacional – Facultad Regional Mendoza (CONICET/CNEA), Mendoza, Argentina*
[7]: *Instituto de Tecnologías en Detección y Astropartículas (CNEA, CONICET, UNSAM), Buenos Aires, Argentina*
[8]: *International Center of Advanced Studies and Instituto de Ciencias Físicas, ECyT-UNSAM and CONICET, Campus Miguelete – San Martín, Buenos Aires, Argentina*
[9]: *Laboratorio Atmósfera – Departamento de Investigaciones en Láseres y sus Aplicaciones – UNIDEF (CITEDEF-CONICET), Argentina*
[10]: *Observatorio Pierre Auger, Malargüe, Argentina*
[11]: *Observatorio Pierre Auger and Comisión Nacional de Energía Atómica, Malargüe, Argentina*
[12]: *Universidad Tecnológica Nacional – Facultad Regional Buenos Aires, Buenos Aires, Argentina*
[13]: *University of Adelaide, Adelaide, S.A., Australia*
[14]: *Université Libre de Bruxelles (ULB), Brussels, Belgium*
[15]: *Vrije Universiteit Brussels, Brussels, Belgium*
[16]: *Centro Brasileiro de Pesquisas Fisicas, Rio de Janeiro, RJ, Brazil*
[17]: *Centro Federal de Educação Tecnológica Celso Suckow da Fonseca, Petropolis, Brazil*
[18]: *Instituto Federal de Educação, Ciência e Tecnologia do Rio de Janeiro (IFRJ), Brazil*
[19]: *Universidade de São Paulo, Escola de Engenharia de Lorena, Lorena, SP, Brazil*
[20]: *Universidade de São Paulo, Instituto de Física de São Carlos, São Carlos, SP, Brazil*
[21]: *Universidade de São Paulo, Instituto de Física, São Paulo, SP, Brazil*
[22]: *Universidade Estadual de Campinas, IFGW, Campinas, SP, Brazil*
[23]: *Universidade Estadual de Feira de Santana, Feira de Santana, Brazil*
[24]: *Universidade Federal de Campina Grande, Centro de Ciencias e Tecnologia, Campina Grande, Brazil*
[25]: *Universidade Federal do ABC, Santo André, SP, Brazil*
[26]: *Universidade Federal do Paraná, Setor Palotina, Palotina, Brazil*
[27]: *Universidade Federal do Rio de Janeiro, Instituto de Física, Rio de Janeiro, RJ, Brazil*
[28]: *Universidade Federal do Rio de Janeiro (UFRJ), Observatório do Valongo, Rio de Janeiro, RJ, Brazil*
[29]: *Universidade Federal Fluminense, EEIMVR, Volta Redonda, RJ, Brazil*
[30]: *Universidad de Medellín, Medellín, Colombia*
[31]: *Universidad Industrial de Santander, Bucaramanga, Colombia*
[32]: *Charles University, Faculty of Mathematics and Physics, Institute of Particle and Nuclear Physics, Prague, Czech Republic*
[33]: *Institute of Physics of the Czech Academy of Sciences, Prague, Czech Republic*
[34]: *Palacky University, Olomouc, Czech Republic*
[35]: *CNRS/IN2P3, IJCLab, Université Paris-Saclay, Orsay, France*
[36]: *Laboratoire de Physique Nucléaire et de Hautes Energies (LPNHE), Sorbonne Université, Université de Paris, CNRS-IN2P3, Paris, France*
[37]: *Univ. Grenoble Alpes, CNRS, Grenoble Institute of Engineering Univ. Grenoble Alpes, LPSC-IN2P3, 38000 Grenoble, France*
[38]: *Université Paris-Saclay, CNRS/IN2P3, IJCLab, Orsay, France*
[39]: *Bergische Universität Wuppertal, Department of Physics, Wuppertal, Germany*
[40]: *Karlsruhe Institute of Technology (KIT), Institute for Experimental Particle Physics, Karlsruhe, Germany*
[41]: *Karlsruhe Institute of Technology (KIT), Institut für Prozessdatenverarbeitung und Elektronik, Karlsruhe, Germany*
[42]: *Karlsruhe Institute of Technology (KIT), Institute for Astroparticle Physics, Karlsruhe, Germany*
[43]: *RWTH Aachen University, III. Physikalisches Institut A, Aachen, Germany*
[44]: *Universität Hamburg, II. Institut für Theoretische Physik, Hamburg, Germany*
[45]: *Universität Siegen, Department Physik – Experimentelle Teilchenphysik, Siegen, Germany*
[46]: *Gran Sasso Science Institute, L'Aquila, Italy*
[47]: *INFN Laboratori Nazionali del Gran Sasso, Assergi (L'Aquila), Italy*
[48]: *INFN, Sezione di Catania, Catania, Italy*

[49]: *INFN, Sezione di Lecce, Lecce, Italy*
[50]: *INFN, Sezione di Milano, Milano, Italy*
[51]: *INFN, Sezione di Napoli, Napoli, Italy*
[52]: *INFN, Sezione di Roma "Tor Vergata", Roma, Italy*
[53]: *INFN, Sezione di Torino, Torino, Italy*
[54]: *Istituto di Astrofisica Spaziale e Fisica Cosmica di Palermo (INAF), Palermo, Italy*
[55]: *Osservatorio Astrofisico di Torino (INAF), Torino, Italy*
[56]: *Politecnico di Milano, Dipartimento di Scienze e Tecnologie Aerospaziali , Milano, Italy*
[57]: *Università del Salento, Dipartimento di Matematica e Fisica "E. De Giorgi", Lecce, Italy*
[58]: *Università dell'Aquila, Dipartimento di Scienze Fisiche e Chimiche, L'Aquila, Italy*
[59]: *Università di Catania, Dipartimento di Fisica e Astronomia "Ettore Majorana", Catania, Italy*
[60]: *Università di Milano, Dipartimento di Fisica, Milano, Italy*
[61]: *Università di Napoli "Federico II", Dipartimento di Fisica "Ettore Pancini", Napoli, Italy*
[62]: *Università di Palermo, Dipartimento di Fisica e Chimica "E. Segrè", Palermo, Italy*
[63]: *Università di Roma "Tor Vergata", Dipartimento di Fisica, Roma, Italy*
[64]: *Università Torino, Dipartimento di Fisica, Torino, Italy*
[65]: *Benemérita Universidad Autónoma de Puebla, Puebla, México*
[66]: *Unidad Profesional Interdisciplinaria en Ingeniería y Tecnologías Avanzadas del Instituto Politécnico Nacional (UPIITA-IPN), México, D.F., México*
[67]: *Universidad Autónoma de Chiapas, Tuxtla Gutiérrez, Chiapas, México*
[68]: *Universidad Michoacana de San Nicolás de Hidalgo, Morelia, Michoacán, México*
[69]: *Universidad Nacional Autónoma de México, México, D.F., México*
[70]: *Universidad Nacional de San Agustin de Arequipa, Facultad de Ciencias Naturales y Formales, Arequipa, Peru*
[71]: *Institute of Nuclear Physics PAN, Krakow, Poland*
[72]: *University of Łódź, Faculty of High-Energy Astrophysics,Łódź, Poland*
[73]: *Laboratório de Instrumentação e Física Experimental de Partículas – LIP and Instituto Superior Técnico – IST, Universidade de Lisboa – UL, Lisboa, Portugal*
[74]: *"Horia Hulubei" National Institute for Physics and Nuclear Engineering, Bucharest-Magurele, Romania*
[75]: *Institute of Space Science, Bucharest-Magurele, Romania*
[76]: *Center for Astrophysics and Cosmology (CAC), University of Nova Gorica, Nova Gorica, Slovenia*
[77]: *Experimental Particle Physics Department, J. Stefan Institute, Ljubljana, Slovenia*
[78]: *Universidad de Granada and C.A.F.P.E., Granada, Spain*
[79]: *Instituto Galego de Física de Altas Enerxías (IGFAE), Universidade de Santiago de Compostela, Santiago de Compostela, Spain*
[80]: *IMAPP, Radboud University Nijmegen, Nijmegen, The Netherlands*
[81]: *Nationaal Instituut voor Kernfysica en Hoge Energie Fysica (NIKHEF), Science Park, Amsterdam, The Netherlands*
[82]: *Stichting Astronomisch Onderzoek in Nederland (ASTRON), Dwingeloo, The Netherlands*
[83]: *Universiteit van Amsterdam, Faculty of Science, Amsterdam, The Netherlands*
[84]: *Case Western Reserve University, Cleveland, OH, USA*
[85]: *Colorado School of Mines, Golden, CO, USA*
[86]: *Department of Physics and Astronomy, Lehman College, City University of New York, Bronx, NY, USA*
[87]: *Michigan Technological University, Houghton, MI, USA*
[88]: *New York University, New York, NY, USA*
[89]: *University of Chicago, Enrico Fermi Institute, Chicago, IL, USA*
[90]: *University of Delaware, Department of Physics and Astronomy, Bartol Research Institute, Newark, DE, USA*
[91]: *University of Wisconsin-Madison, Department of Physics and WIPAC, Madison, WI, USA*
: —–
[a]: *Louisiana State University, Baton Rouge, LA, USA*
[b]: *Institut universitaire de France (IUF), France*
[c]: *also at University of Bucharest, Physics Department, Bucharest, Romania*
[d]: *School of Physics and Astronomy, University of Leeds, Leeds, United Kingdom*
[e]: *now at Agenzia Spaziale Italiana (ASI). Via del Politecnico 00133, Roma, Italy*
[f]: *Fermi National Accelerator Laboratory, Fermilab, Batavia, IL, USA*
[g]: *now at Graduate School of Science, Osaka Metropolitan University, Osaka, Japan*
[h]: *now at ECAP, Erlangen, Germany*
[i]: *Max-Planck-Institut für Radioastronomie, Bonn, Germany*
[j]: *also at Kapteyn Institute, University of Groningen, Groningen, The Netherlands*
[k]: *Colorado State University, Fort Collins, CO, USA*
[l]: *Pennsylvania State University, University Park, PA, USA*

(Dated: November 1, 2023)

The *Auger Engineering Radio Array* (AERA), part of the Pierre Auger Observatory, is currently the largest array of radio antenna stations deployed for the detection of cosmic rays, spanning an area of $17 \, \mathrm{km}^2$ with 153 radio stations. It detects the radio emission of extensive air showers produced

by cosmic rays in the $30 - 80\,\mathrm{MHz}$ band. Here, we report the AERA measurements of the *depth of the shower maximum* ($X_{\max}$), a probe for mass composition, at cosmic-ray energies between $10^{17.5}$ to $10^{18.8}\,\mathrm{eV}$, which show agreement with earlier measurements with the fluorescence technique at the Pierre Auger Observatory. We show advancements in the method for radio $X_{\max}$ reconstruction by comparison to dedicated sets of CORSIKA/CoREAS air-shower simulations, including steps of reconstruction-bias identification and correction, which is of particular importance for irregular or sparse radio arrays. Using the largest set of radio air-shower measurements to date, we show the radio $X_{\max}$ resolution as a function of energy, reaching a resolution better than $15\,\mathrm{g\,cm^{-2}}$ at the highest energies, demonstrating that radio $X_{\max}$ measurements are competitive with the established high-precision fluorescence technique. In addition, we developed a procedure for performing an extensive data-driven study of systematic uncertainties, including the effects of acceptance bias, reconstruction bias, and the investigation of possible residual biases. These results have been cross-checked with air showers measured independently with both the radio and fluorescence techniques, a setup unique to the Pierre Auger Observatory.
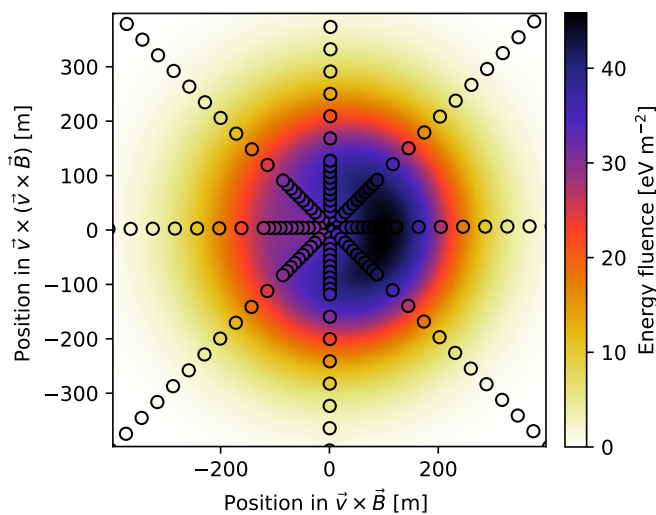
I. INTRODUCTION

FIG. 1. Example of a footprint of the radio emission on the ground for a simulated air shower with an energy of $8.2 \cdot 10^{17}\,\mathrm{eV}$, a zenith angle of $50.2°$, and a depth of the shower maximum of $749\,\mathrm{g\,cm^{-2}}$. The strength of the emission is evaluated at simulated antenna positions (markers) and interpolated in between for visibility (background). The footprint has been projected into the *shower plane*, i.e., tilted into the plane perpendicular to the shower axis $\vec{v}$ and rotated to project the magnetic field $\vec{B}$ along the x-axis.

The measurement of *ultra-high-energy cosmic rays* (UHECRs) relies on the detection of the products of extensive air showers that are initiated when cosmic rays impact Earth's atmosphere. The study of these air showers allows one to extract their properties and thereby reconstruct important observables, such as the arrival direction of the cosmic-ray primary, its energy, and its particle type. Knowing the particle type is key to understanding the nature and origin of cosmic rays. This is of particular interest in the energy range between 10^{17} to $10^{19}\,\mathrm{eV}$ where the cosmic-ray flux is expected to transition from having Galactic to extragalactic sources (see for example the review [1]. In the *transition region* a change in mean mass of the primaries, their *mass composition*,
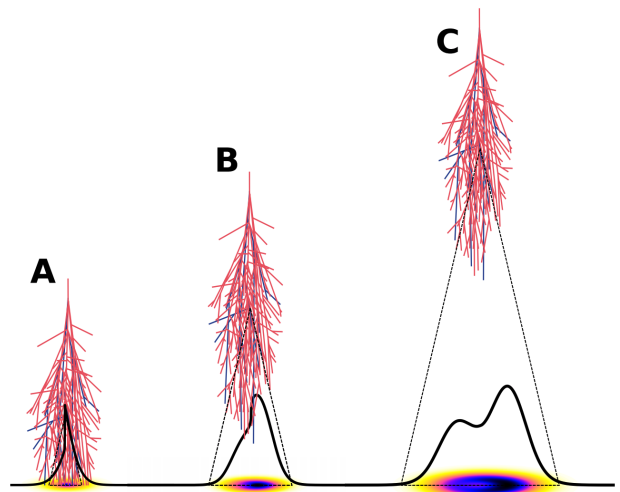
FIG. 2. Schematic view of three air showers that started at different heights in the atmosphere, and their radio emission footprints on the ground. It illustrates that the depth of the shower maximum affects the radio emission footprint both in width and general shape. The asymmetry is a consequence of how the geomagnetic and charge excess radio emission mechanisms interfere during the shower development. This figure has been previously published in [15].

could help disentangle source contributions.

The past decades have seen major improvements to the detection of extensive air showers and the reconstruction of air-shower parameters. Though typically this has up until now been the domain of direct particle detection and the observation of air-Cherenkov or fluorescence light, the last two decades also saw the detection of radio emission from air showers coming to maturity [2–8]. For reviews on the recent progress see e.g. [9, 10]. This is important as the radio technique has the advantage of a near-100% duty cycle and relatively low-cost hardware, while still performing precision measurements of the electromagnetic part of the shower. In the extensive air shower, changing currents, caused by charged particles moving under the influence of the Earth's magnetic field (geomagnetic emission) and by the ionization of the

surrounding atmospheric medium (charge excess emission), lead to electromagnetic radiation, predominantly in the MHz to GHz frequency band. Using an array of radio antennas on the ground, the radio emission footprint can then be measured. An example of a simulated radio footprint on the ground is shown in Fig. 1. The radio footprint shape depends strongly on particle type and can thus be used to probe the cosmic-ray mass composition. A heavier primary nucleus (which acts roughly as a superposition of multiple lower-energy nucleons) will, on average, interact higher up in the atmosphere and hence produce a wider footprint on the ground than a lighter primary particle. This is illustrated in Fig. 2. The particle type itself is not a direct observable, but the atmospheric depth where the shower is maximally developed, the *depth of the shower maximum* $X_{\max}$, which depends on the particle type, can be related to the shower footprint shape, making $X_{\max}$ a probe for the primary particle type.

Several methods have been used over the past years to reconstruct the particle type from radio signals, most of those relying on determining either the slope, width, or full shape of the *lateral distribution function* (LDF) of the radio footprint to determine $X_{\max}$ [11–15]. In addition, also other methods using for example the slope of the frequency spectrum [16, 17] and shape of the shower wavefront have been attempted [18]. Out of all these methods, the highest resolution in $X_{\max}$ has been thus far achieved by using the LDF of the radio footprint by fitting of simulated air showers to measured air showers [19, 20].

In this work, the simulation-fitting method has been further developed for the *Auger Engineering Radio Array* (AERA), by accounting for the effects of the sparse (compared to other radio experiments) and irregular array of radio stations. Also, a thorough investigation of systematic uncertainties has been made. We present the details of the $X_{\max}$ reconstruction method and quantify the resolution as a function of cosmic-ray energy. Next, we apply the method to the set of air showers measured by AERA to determine the distributions of $X_{\max}$ and interpret this in terms of the cosmic-ray mass composition. We then compare the composition to the results of the *fluorescence detector* (FD) at the Pierre Auger Observatory. Furthermore, we use a subset of air showers, simultaneously measured and independently reconstructed with both AERA and FD to directly evaluate our method and place bounds on the total systematic uncertainty between the two $X_{\max}$ detection techniques.

This paper will start with a description of the AERA air-shower reconstruction and the selection of showers in Sec. II. Then, the $X_{\max}$ reconstruction method will be described in Sec. III. In Sec. IV we make an inventory of systematic uncertainties on the reconstruction of the $X_{\max}$ distribution of the selected air showers. The resolution with which $X_{\max}$ is reconstructed is then shown in Sec. V. Finally, the resulting $X_{\max}$ distribution as measured by AERA will be presented in Sec. VI.
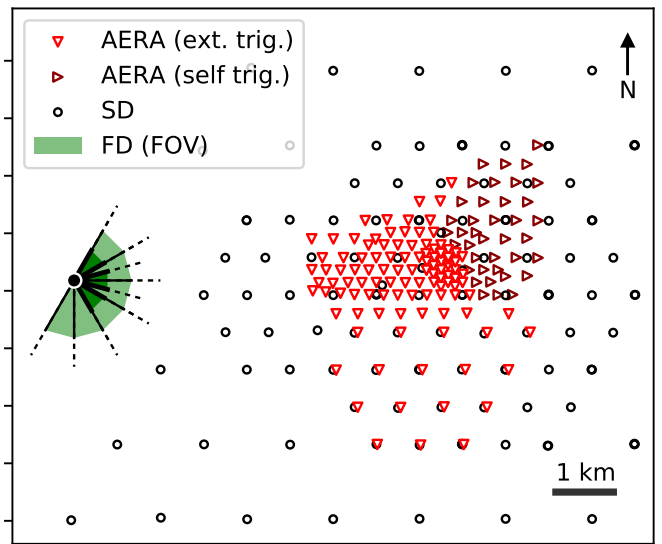
FIG. 3. Layout of the AERA stations (triangles), marked with whether they are externally- or self-triggered. Also shown is part of the SD array of water-Cherenkov detectors (circles) and the *field of view* (FOV) of one of the FD telescope sites located near AERA. The FD contains 6 regular telescope bays (light green) and in addition 3 bays (dark green) looking at higher elevations. Scale and orientation of the layout are indicated with markers.

In an accompanying publication [21] these results are discussed in the context of the larger field of other measurement techniques and experiments.

II. AERA DATA RECONSTRUCTION

The Pierre Auger Observatory [22] is located near the town of Malargüe in Argentina. It aims at detecting UHECRs up to the highest energies. The observatory covers an area of $3000\,\mathrm{km}^2$, making it the largest of its kind in the world. The main components of the observatory are an array of 1660 *water-Cherenkov detectors* (WCDs), also called the *surface detector* (SD), and 27 fluorescence telescopes (known as the *fluorescence detector*, FD) that overlook the SD. Located near one of the FD sites and within the SD grid is also an array of radio detectors (AERA) [23]. This radio array consists of 153 autonomous stations, each with two orthogonally placed dipole antennas, that measure the spectrum between 30 and 80 MHz, sampling the signal roughly every 5 ns. The measured voltage signals in the antenna arms are converted to an electric field $\vec{E}(t)$ from which we calculate the integrated signal per unit area, conventionally called the *energy fluence* $u\,[\mathrm{eV/m}^2]$. Part of the measured energy fluence will be from the background noise that will need to be subtracted. One can assume that before the cosmic-ray signal arrives, or long after the cosmic-ray pulse has passed, that the electric field time trace also represents the noise during the time of the signal.

FIG. 4. Distributions of shower energy (left), and the azimuth and zenith angles of the shower arrival direction (center and right, respectively) for the pre-selection of 2153 high-quality AERA showers (blue), the showers for which $X_{\max}$ was reconstructed successfully with our method (gray), and the sample of showers after acceptance and reconstruction cuts are applied (green). The cosmic-ray energy spectrum as measured by Auger SD [24] (gray dashed line) is scaled to the energy distribution of AERA to illustrate the level of completeness of the AERA event set at the higher energies.
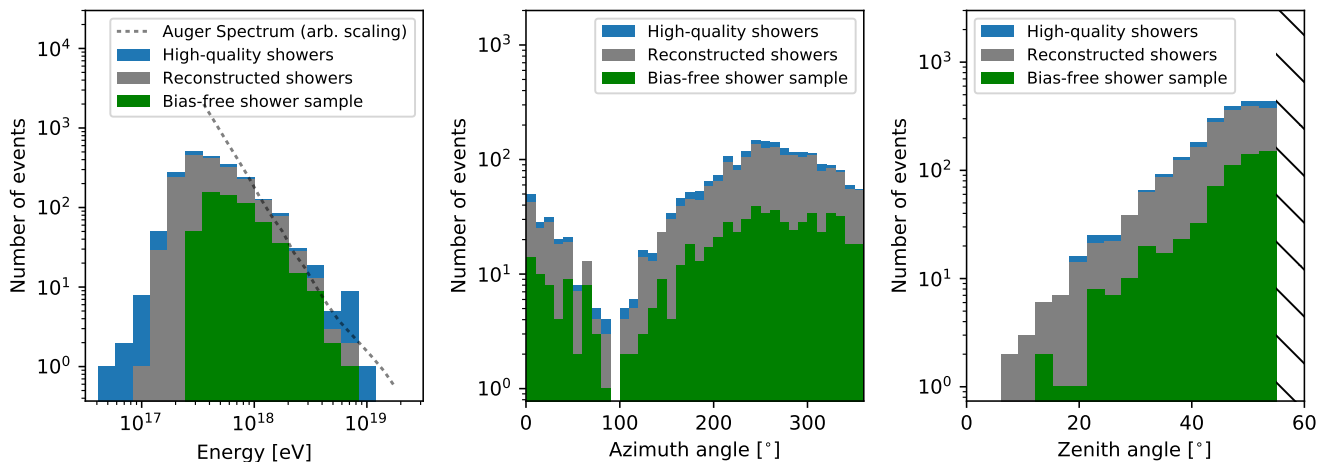
The energy fluence can then be calculated as the integral over the time period $[t_1,\, t_N]$ containing the signal, minus the contribution of a pure background time interval $[t_{b,1},\, t_{b,M}]$, where N and M are the respective numbers of samples for the bin size Δt:

$$u = \epsilon_0 c \Delta t \left(\sum_{i=1}^{N} \left| \vec{E}(t_i) \right|^2 - \frac{t_N - t_1}{t_{b,M} - t_{b,1}} \sum_{i=1}^{M} \left| \vec{E}(t_{b,i}) \right|^2 \right), \tag{1}$$

where ϵ_0 is the vacuum permittivity and c the speed of light.

The spacing between radio stations varies between $144\,\mathrm{m}$ and $750\,\mathrm{m}$ (see Fig. 3) and the array spans a total area of $17\,\mathrm{km}^2$. While the radio stations can be triggered on the radio signals themselves, in this work we make use of just the external trigger provided by the SD such that we also directly have the measurement of shower energy at our disposal. Consequently, the dark red part of the radio array, shown in the upper right part in Fig. 3, is a subset of detectors that operate in a self-triggering mode and consequently are not used in this analysis.

The water-Cherenkov detectors are spaced on a triangular grid of $750\,\mathrm{m}$ that overlaps with the AERA station grid. Because the radio station spacing is typically much smaller, the estimation of the shower core position and arrival direction is made with the information of cosmic-ray signals in the AERA stations.

From the 7 years of AERA measurements (2013/04 - 2019/11), we select air-shower candidate events that were triggered by SD, which meet the requirement of a certain quality in terms of clustering of triggered SD stations [39, p. 79]. Additionally, we select on the events where at least 5 AERA stations have measured a signal with a signal-to-noise ratio above 10 (the signal is defined here as the square of the maximum of the Hilbert envelope of the electric field and the noise as the square of

TABLE I. The number of air-shower events remaining after applying the selection criteria sequentially. η shows the fraction of showers remaining after each of the cuts. The three sections correspond to the three sets of events in Fig. 4.

Quality cut criteria	Events	$\eta[\%]$
High-quality shower pre-selection (Sec. II):		
Air-shower candidates	9336	-
SD zenith angle $< 55°$	4874	52.2
SD trigger quality	2832	58.1
AERA zenith angle $< 55°$	2762	97.5
Δ AERA and SD arrival direction $< 10°$	2733	99.0
No thunderstorm conditions	2160	79.0
Δ AERA and SD core position $< 400\,\mathrm{m}$	2153	99.7
Reconstructed air showers (Sec. III):		
Insufficient high-SNR sim. radio signals	1967	91.4
High-quality $X_{\max}$ parabola fit	1725	87.7
Valid $X_{\max}$ uncertainty and bias estimation	1625	94.2
Bias-free shower sample (Sec. IV):		
$E \geq 10^{17.5}\,\mathrm{eV}$	1107	68.1
Acceptance cut	594	53.7

the RMS of the electric field in a time window away from the signal), a lower limit set by the requirements for the $X_{\max}$ reconstruction in Sec. III. As part of these criteria, an algorithm was implemented to reject stations from the shower reconstruction in case of hardware failures or excessive *radio-frequency interference* (RFI) background signals, which is monitored every $100\,\mathrm{seconds}$. We also limit the data set to showers arriving from within $55°$ of the zenith. Firstly, because the reconstruction at higher inclinations is currently an active field of study [26, 27], and secondly, because sensitivity to $X_{\max}$ decreases for higher inclinations since the emission region will be more distant. We require both the SD and AERA arrival direction reconstruction to find angles below $55°$ and also

require agreement between the arrival direction within $10°$ and core position within $400\,m$. This acts only as a rejection of outlier values due to bad reconstructions; the arrival direction and core position reconstruction are much better than this (about $1°$ and $50\,m$, respectively, for SD and similar or smaller for AERA) [28, 29]. Furthermore, periods of enhanced atmospheric electric field conditions, such as occur during times of thunderstorms, are removed from the data set. To be conservative, events are also rejected if no electric field information was available (accounting for half of the events that are rejected in this step). This results in a pre-selected set of 2153 showers in the energy range of 10^{17} to 10^{19} eV, the lower limit being set by the detection threshold above the radio background level and the upper limit being exposure-limited. In Table I we list these cut criteria and the number of events after each cut. In Fig. 4 we show the distribution of these air showers as a function of the shower energy (left), and the azimuth and zenith angles of the arrival direction (center and right, respectively). Indicated in blue is the pre-selected set of showers as described above. The gray and green elements in the figure refer to further quality cuts in the reconstruction of $X_{\max}$ (gray) and selection of a bias-free sample (green) as will be described in Sec. IV. To illustrate the completeness of the data set, at least at higher energies, the cosmic-ray flux as measured by the Pierre Auger Observatory [24] has been superimposed and re-scaled to the AERA shower distribution.

Note that the radio signal strength depends on the Lorentz force $F \sim \vec{v} \times \vec{B}$, and thus on the angle between the arrival direction of the shower $\vec{v}$ with respect to the Earth's magnetic field $\vec{B}$, hence the increased suppression of the detected showers as the azimuth angle approached (approximately) $90°$ and the arrival direction becomes more aligned with the magnetic field.

There is a small overlap in the effective field of view of AERA and FD, such that for a subset of 53 showers in the set of selected showers for AERA also an independent high-quality FD shower reconstruction is available. The number is mainly limited by the distance and different energy dependent apertures of AERA and FD, and the FD duty cycle. We will use these 53 showers in Sec. IV for an independent check on the $X_{\max}$ reconstruction on an event-by-event basis.

III. RECONSTRUCTION METHOD FOR $X_{\max}$

The method to reconstruct the depth of the shower maximum that we use in this work is based on the method developed for LOFAR [19, 20] where a set of Monte-Carlo (MC) air-shower simulations is generated based on the basic reconstructed properties of a measured air shower such as cosmic-ray energy and arrival direction. The depth of the shower maximum $X_{\max}$, is affected by shower-to-shower fluctuations and thus similarly varies for each of the simulations. The sensitivity of the radio

signals to $X_{\max}$ is then used to match the radio signals between measurement and simulations to reconstruct the $X_{\max}$ value of the measured air shower. We use the air-shower simulation code CORSIKA v7.7100 [30] with radio extension CoREAS [6] and QGSJetII-04 [31] as our high-energy hadronic interaction model. We include several higher-order effects to simulate the individual measured air showers as precisely as possible. We include the *Global Data Assimilation System* (GDAS) atmospheric model [32, 33] for our time and location-dependent air density and refractive index modelling. A time-variable geomagnetic field model [34] is also used because the majority of the emission being driven by the magnetic field, which changed slightly over the several years of AERA data used in this work. We model the simulated stations to lie on the sloped plane of AERA and add several concentric rings of 'virtual' stations such that we can interpolate the energy fluences with higher precision between AERA station positions. This is done because the core position of the shower is only known to the order of $20\,m$ and, when comparing the simulated and measured radio signals, we shift the simulated footprints to correct for the offset caused by this uncertainty.

As input for the shower simulations we use the shower energy from SD. All showers in the data set are triggered by the SD and hence the SD energy measurement is available for each event. For the shower core position and arrival direction, we use the reconstruction from AERA. The stochastic nature of particle interactions in the air shower leads to shower-to-shower fluctuation in $X_{\max}$ such that this parameter can be described by a Gumbel distribution [35]. We create an ensemble of 27 simulations for each of the 2153 selected air showers: 15 induced by protons and 12 induced by iron nuclei (intermediate-mass particles are not used as it has been shown to not be necessary [36]). We use more proton showers since these cover a larger range in $X_{\max}$. These primaries and quantities are selected to cover the true distribution of $X_{\max}$), including the tails of the $X_{\max}$ distributions, by varying the initial seeds and height of the first interaction of the primary cosmic ray, while keeping all other input parameters identical. In this way, when comparing the simulated and measured radio signals, we can determine the $X_{\max}$ value which best describes the measured signals of the air shower.

For each shower we quantify the quality of the match between the measured and the simulated radio signals by defining a chi-squared quantity based on the energy fluence u and the corresponding uncertainty σ_u of the radio stations:

$$\chi^2 = \sum_{\text{stations}} \frac{\left(u_{\text{measured}} - S \cdot u_{\text{simulated}}(\vec{r}_{\text{shift}})\right)^2}{\sigma^2_{u_{\text{measured}}}}. \quad (2)$$

The simulated energy fluences $u_{\text{simulated}}$ are calculated by applying the AERA antenna response to the pure simulated signals and then reconstructing them as if they were actual measured signals [37] (no noise is
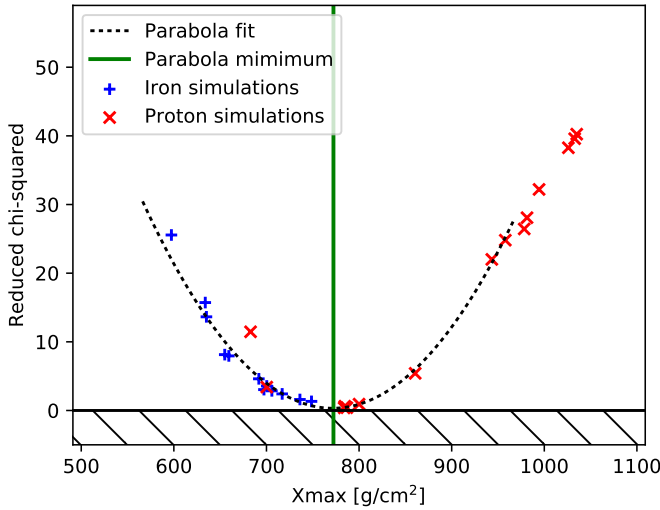
FIG. 5. Parabola fit (dashed black line) to the reduced chi-squared values between a measured shower and each of the simulated showers for this event (blue and red markers) [see Eq. (2)] as a function of the true MC $X_{\max}$ values for each simulation. The minimum of the parabola (green line) is an estimator for the $X_{\max}$ value of the measured shower. This measured shower has an energy of $8.2 \cdot 10^{17}$ eV, a zenith angle of $50.2°$, and reconstructed $X_{\max} = 763 \pm 19\,\mathrm{g\,cm^{-2}}$. It has been chosen as a representative shower falling in the middle of the AERA energy range (Fig. 4, left), being close to the most common zenith angle (Fig. 4, right), and having a typical $X_{\max}$ resolution (Fig. 14).

added to the simulated signals since we would have to remove it again to calculate the energy fluence, as in Eq. 1, needlessly reducing precision. The uncertainty on $X_{\max}$ reconstruction due to noise is accounted for later in this section). In the chi-squared measure, we account for the possible systematic uncertainties from the air-shower simulations and the uncertainty on the reconstruction of the shower energy by introducing a scaling parameter S between measured and simulated energy fluences. We also account for the uncertainty on the reconstruction of the shower core position with a core shifting parameter $\vec{r}_{\mathrm{shift}}$. Suitable starting values for the core shift are taken from either an initial fitting procedure [15] or a barycenter calculation. Both free parameters are shared between all simulations for the event under consideration (because a measured shower and its corresponding simulations have just a single core offset and energy scaling between them).

The chi-squared values for each of the shower simulations as a function of the true MC $X_{\max}$ values of those shower simulations can be fitted (locally) with a parabola function as is illustrated in Fig. 5 such that the $X_{\max}$ value at the minimum of the parabola fit $X_{\max}^{\mathrm{parabola}}$ acts as an estimator for the $X_{\max}$ value of the measured shower. The minimum is found by an iterative procedure where the free parameter space of S and $\vec{r}_{\mathrm{shift}}$ is searched for a global minimum in χ^2. Checks are built into the procedure such that the minimum is in fact a
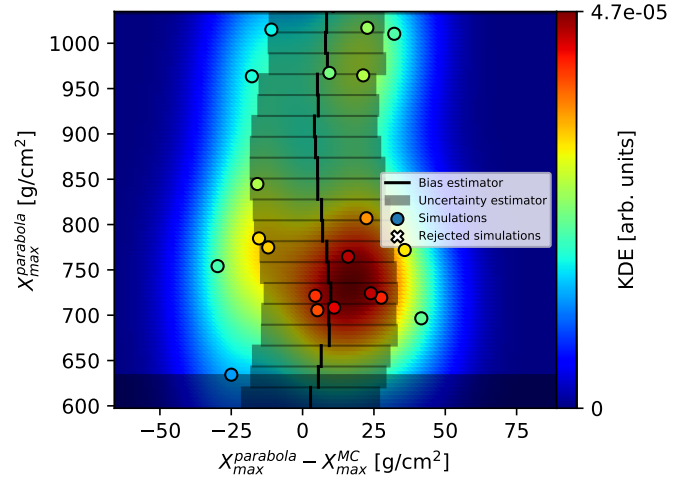

FIG. 6. The parabola $X_{\max}$ values reconstructed for the set of simulations of a single measured air shower (same as Fig 5), as a function of the deviation to the true MC $X_{\max}$ values (dots). A kernel density estimation (background color) is made to estimate the probability density function of the difference at each $X_{\max}^{\mathrm{parabola}}$ value. From this, a mean $\Delta X_{\max,1}^{\mathrm{KDE}}$ and width $\delta X_{\max,1}^{\mathrm{KDE}}$ is derived as first-order estimation of bias an estimation of uncertainty in the $X_{\max}^{\mathrm{parabola}}$ estimator (gray bands at regular intervals). The shaded band at the bottom illustrates the shallowest $X_{\max}$ that can be reconstructed such that the parabola minimum remains contained well within the MC $X_{\max}$ range. The bias correction procedure corrects for bias introduced by this restriction.
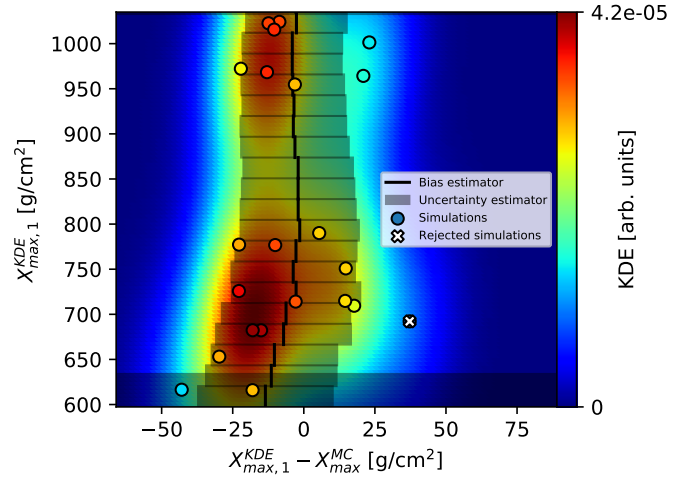
FIG. 7. Second-order bias correction $\Delta X_{\max,2}^{\mathrm{KDE}}$ and total uncertainty $\delta X_{\max,2}^{\mathrm{KDE}}$ after including the effects of a free core and free energy scaling in the minimization procedure. Once again the same event is used as in Fig. 5 and Fig. 6.

global minimum (using a basin-hopping minimizer [38] and an additional coarse full-parameter space search), and that the parabola fit is well-behaved. We test the validity of this procedure by evaluating this with the reconstruction of each of the simulated showers under realistic ambient noise conditions (from periodic noise mea-

surements with our stations), by leaving out that specific simulation and then minimizing χ^2 using the other 26 simulations belonging to that particular air-shower event. The minimization then provides S and $\vec{r}_{\text{shift}}$ parameters for evaluation. We reconstruct $S = 1$ within an offset of $(0.9 \pm 0.4)\%$ and a spread of $(23.4 \pm 0.1)\%$. The bias is negligibly small and the uncertainty is primarily driven by the propagation of the uncertainty on the radio signal itself. The free parameter for the core shift we determine to have a minor bias of $(0.4 \pm 0.2)\,\text{m}$ and the spread is found to be $(20.6 \pm 0.2)\,\text{m}$, which is on the same order as the core position resolution of AERA. Hence, the minimization algorithm used to determine the best-fit between measured (or the simulated ones mimicking real measurements) and simulated showers does not introduce any additional biases in the free parameters.

The resolution and possible bias of the parabola-X_{max} reconstruction procedure is evaluated by reconstructing the $X_{\text{max}}^{\text{parabola}}$ values of each of the 27 simulated showers, that we have for each measured shower, and comparing these reconstructions to their true Monte Carlo values $X_{\text{max}}^{\text{MC}}$. An example of this procedure is shown in Fig. 6. It shows the difference between the $X_{\text{max}}^{\text{parabola}}$ and $X_{\text{max}}^{\text{MC}}$ values for each of the simulations (points) as a function of $X_{\text{max}}^{\text{parabola}}$. Note that simulations with a bad χ^2 probability for the parabola fit are shown as rejected (crosses, see Fig. 7) and simulations that failed to reconstruct are not shown (the resulting effect on the detector sensitivity to X_{max} is quantified in Sec. IV). The spread along the horizontal axis is not necessarily a constant value for any $X_{\text{max}}^{\text{parabola}}$ and, in addition, there can be a bias that depends on $X_{\text{max}}^{\text{parabola}}$ itself. The main reason for this is that the constraining power on X_{max} is determined by the amount and quality of radio signals for a particular air shower and these quantities change with X_{max}. In addition, the parabola fit in the estimation of $X_{\text{max}}^{\text{parabola}}$ will be more difficult to make when the chi-squared minimum is near the edges of the range of $X_{\text{max}}^{\text{MC}}$ values. As a consequence, the very low X_{max} values will often be overestimated and the very high values often underestimated. Because of this inherent bias in this estimator, we implement steps to mitigate this. We model the spread and bias of the difference in $X_{\text{max}}^{\text{parabola}}$ versus $X_{\text{max}}^{\text{MC}}$ by determining the *kernel density estimator* (KDE) for the simulated points (colored background in Fig. 6). A KDE is a method to estimate a smooth probability density distribution based on substituting discrete points by smooth functions (Gaussian kernels). We extract from this the mean and 1σ spread at any desired $X_{\text{max}}^{\text{parabola}}$ value (illustrated with regularly spaced black bars). A shift from zero on the horizontal axis then indicates the bias as a function of $X_{\text{max}}^{\text{parabola}}$ and the spread of the points provides the uncertainty of the reconstruction. Note that for the spread we have taken into account that the bandwidth of the KDE broadens the spread and we have corrected for this such that the uncertainty on X_{max} that we determine is truly a 1σ error with respect to the spread in MC X_{max} values.

We perform this procedure in two steps to disentangle, in a more stable way, the effects of the intrinsic uncertainties of our X_{max} reconstruction method and the uncertainties that can arise from the uncertainties on the core position and shower energy (the two free parameters in [Eq. (2)]) that are inherent to just the measured air showers.

In the first step we fix the shower core position and energy scaling parameters to the true Monte-Carlo values such that we can calculate the KDE (Fig. 6) to identify and correct for any bias in the X_{max} estimation

$$\Delta X_{\text{max},1}^{\text{KDE}} \equiv X_{\text{max}}^{\text{parabola}} - X_{\text{max}}^{\text{MC}} \tag{3}$$

caused by the parabola X_{max} estimation itself. This then provides an improved, *first-order bias-corrected*, estimator for X_{max}

$$X_{\text{max},1}^{\text{KDE}} \equiv X_{\text{max}}^{\text{parabola}} - \Delta X_{\text{max},1}^{\text{KDE}}. \tag{4}$$

In the second step, the X_{max} reconstruction is repeated, but now performed including the 2 free parameters. In this way, we can separately identify and correct for any X_{max}-reconstruction bias originating from the uncertainties on the measured core position and shower energy that were used as input parameters for the COR-SIKA simulations. For this we look at the $X_{\text{max},1}^{\text{KDE}}$ estimator (i.e., after the first KDE-correction step) for each reconstructed simulation, compare this to the true MC values as before, model it again with a KDE, and as before extract bias and uncertainty estimators. The second-order bias correction is then given by

$$\Delta X_{\text{max},2}^{\text{KDE}} \equiv \Delta X_{\text{max},1}^{\text{KDE}} - X_{\text{max}}^{\text{MC}} \tag{5}$$

By also applying this correction, our final AERA X_{max} estimator

$$X_{\text{max},2}^{\text{KDE}} \equiv X_{\text{max},1}^{\text{KDE}} - \Delta X_{\text{max},2}^{\text{KDE}} \tag{6}$$

is obtained. The spread in the reconstructed X_{max} values in Fig. 7 provides an estimation of the uncertainty on the X_{max} reconstruction, accounting now for the effects of the full reconstruction procedure as if it was executed on a measured air shower. The spread is extracted from the 1σ region around the bias estimator value in the KDE model (i.e., the region between the 15.87% and 84.13% quantiles). For the remainder of this work the estimators for X_{max} and its uncertainty will be called X_{max} and $\delta_{X_{\text{max}}}$, respectively (for the latter $\delta_{X_{\text{max}}}$ is used instead of $\sigma_{X_{\text{max}}}$ to avoid confusion with the second moment of the X_{max} distribution, $\sigma(X_{\text{max}})$, which will be introduced in Sec. V). For both of the steps of the procedure quality-checks have been built into the procedure to guarantee the bias and uncertainty estimators represent the underlying data correctly. In situations where this was not the case, primarily for showers with lower quality signals, events have been rejected because of having an ill-defined bias and uncertainty (see the 'Valid X_{max} uncertainty and bias estimation' cut in Table I. These quality criteria are described in more detail in [39, p. 163]).

In the end, this procedure provides an end-to-end estimation of $X_{\max}$ uncertainty and bias of the method. However, while the bias correction reduces bias, it can't fully correct it. For example, at the edges of the simulated $X_{\max}$ range the KDE is sparsely populated and, hence, there the method only has a partial ability to correct for biases. One could mitigate this further by doing more simulations, but here we were computationally constrained to 27 simulations per shower. We account for any remaining bias of the reconstruction as systematic uncertainty in Sec. IV.

IV. ACCEPTANCE CUTS AND SYSTEMATIC UNCERTAINTIES

To interpret the distribution of $X_{\max}$ we first implement an acceptance cut such that our set of showers is not biased by selection effects. We first apply a cut in energy at $E = 10^{17.5}$ eV, above which the SD trigger we use to read out AERA is fully efficient [24, 25]. However, not every trigger leads to a high-quality shower in AERA. Hence, we next calculate the detection acceptance for AERA by evaluating the reconstructability of the set of 27 simulated air showers that were created for each measured shower. We implement the condition that the measured shower should have been detected if it had arrived anywhere within the expected range of $X_{\max}$ values as predicted by simulations. Specifically, we require, for any shower we select, that 90% of the $X_{\max}$ values of a Gumbel distribution for both protons and iron nuclei, given the energy of the shower, would be reconstructable by AERA. Removing the events that do not pass the acceptance cut results in 594 showers. Table I lists these quality cut steps and the final distribution of events can be seen in Fig. 4 (green shaded area). Fig. 8, as example, shows the average acceptance (thick green line) for all selected showers with energies between $10^{17.95}$ to $10^{18.10}$ eV and the average Gumbel distributions for the energies of those showers under the assumption of a composition consisting of just protons (solid red), just iron nuclei (solid blue), and the mixed-mass composition as measured by Auger FD [40] (Gumbel parametrization for QGSJetII-04 [41, 42] are used). At these energies AERA is fully efficient up to about $850 \, \mathrm{g\,cm^{-2}}$, after which the efficiency drops slightly for the tail of the proton Gumbel distribution. For the lowest energies this occurs around $800 \, \mathrm{g\,cm^{-2}}$ (not shown).

Although the acceptance is only reduced for extreme $X_{\max}$ values we investigate the systematic uncertainty on the mean and width of our measured $X_{\max}$ distribution that this would cause. For this, we calculate the effect of the acceptance curve on the Gumbel distributions (dashed lines in Fig. 8), which are shown to be modified by less than a few $\mathrm{g\,cm^{-2}}$ compared to the solid lines. The resulting differences in the two moments of the distributions are shown as insets in the figure. This calculation is performed for all energy bins and results in
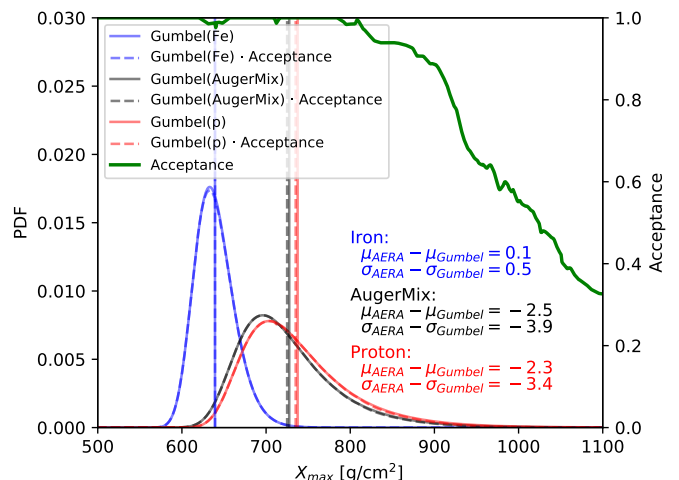

FIG. 8. Calculated acceptance for measured AERA showers in the energy bin from $10^{17.95}$ to $10^{18.10}$ eV (thick green line) and the systematic effect it has on the mean and width of the Gumbel $X_{\max}$ distributions (annotated values in $\mathrm{g\,cm^{-2}}$) for a pure proton mass composition, pure iron mass composition, and the mixed-mass composition as measured by Auger FD [40] (solid red, blue, and black lines). The dashed lines are the distributions convolved with the acceptance. The lines are plotted at 50% opacity since they match closely. Vertical lines show the respective means.

a bias of under $4 \, \mathrm{g\,cm^{-2}}$ and $5 \, \mathrm{g\,cm^{-2}}$ on the mean and width, respectively, when assuming the least favourable composition conditions (see blue bars in Fig. 9). The calculation is included in Appendix A 1.

Next, we also evaluate the bias the $X_{\max}$ reconstruction of individual showers has on the $X_{\max}$ distribution. While Sec. III implemented steps to remove $X_{\max}$ bias, this is not guaranteed to be sufficient, especially for the deepest and shallowest showers, as explained in that section. Hence, the overall effect on the selected set of air showers is evaluated by reconstructing $X_{\max}$ for the air-shower simulations, for which the true MC $X_{\max}$ is known, and calculating the effect the reconstruction would have in the case nature would give us a Gumbel $X_{\max}$ distribution for protons, iron nuclei, or a 50:50 mix of the two. For the mean of the $X_{\max}$ distribution the proton and iron nuclei cases would represent the two extreme cases, since bias occurs mostly for the deepest and shallowest showers. The width of the distribution would be most affected by a mix of proton and iron, hence we evaluate also the case of a 50:50 mix. Fig. 10 shows, as example, the effect on the distribution for the showers in the energy range of $10^{17.95}$ to $10^{18.10}$ eV. The bias in the width and mean of the distributions is taken as systematic uncertainty, again, to be conservative, under the assumption of the composition with the largest bias. We show the results of this as a function of energy in Fig. 9 (red bars) and show the calculation in Appendix A 2.

We furthermore account for systematic uncertainty of the use of the GDAS atmospheric model [19, 43] and the
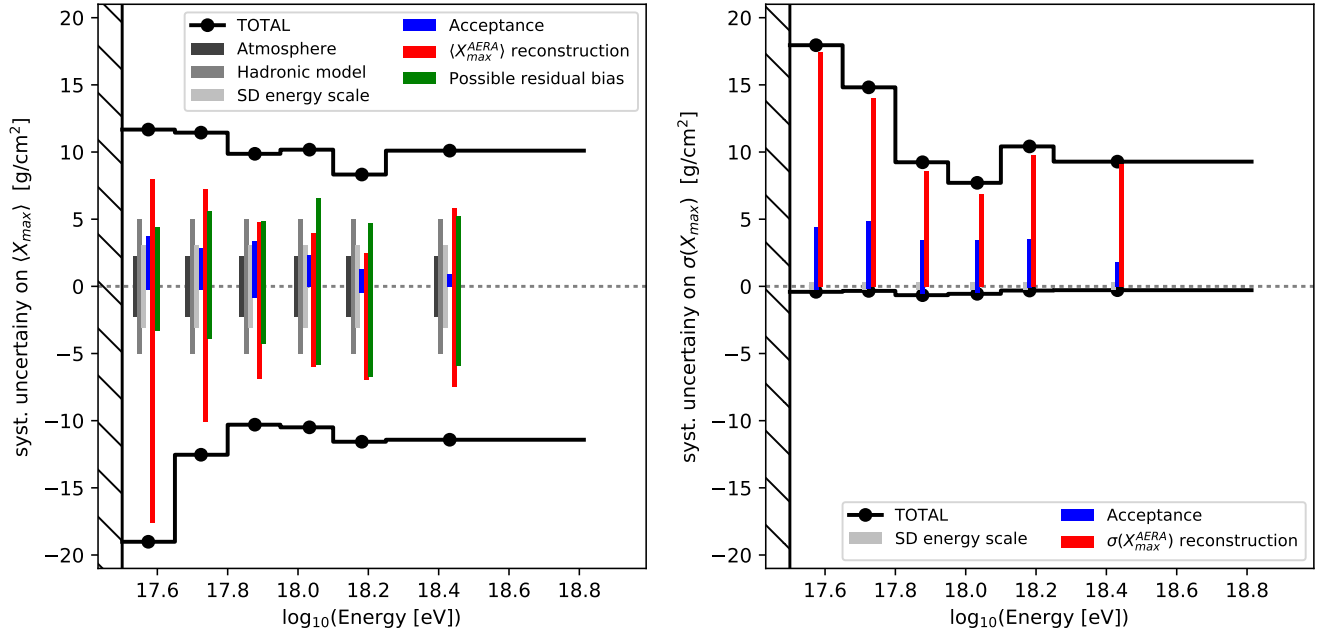
FIG. 9. (Left): Overview of upper and lower values of the systematic uncertainties on the mean of the $X_{\max}$ distribution ($\langle X_{\max} \rangle$). The individual contributions to the total uncertainty are plotted as bars centered in each of the energy bins. The total uncertainty (black lines) is the quadratic sum of the individual contributions. The average energy in each energy bin is shown as black circles. (Right): Overview of systematic uncertainties on the true spread of $X_{\max}$ ($\sigma(X_{\max})$).
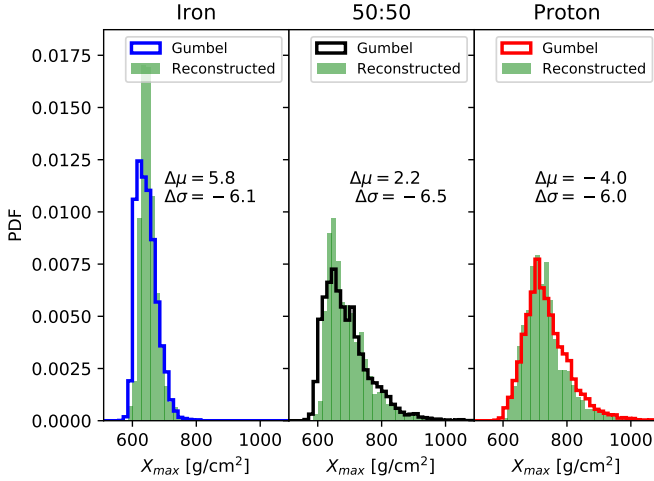

FIG. 10. Calculated systematic uncertainties on the $X_{\max}$ distribution due to the $X_{\max}$ reconstruction method in the energy bin from $10^{17.95}$ to $10^{18.10}$ eV for a pure proton mass composition (left), pure iron nuclei mass composition (right), and a 50:50 mix of the two (center). The Gumbel distributions (solid line) and how AERA would reconstruct this (green area) are plotted. The Gumbel distributions have been convolved with the AERA measurement uncertainties to allow for direct comparison. The difference between the AERA and Gumbel distributions provides an estimation for the systematic bias on the mean and width of the $X_{\max}$ distribution (annotated values in $\mathrm{g\,cm^{-2}}$).

choice of hadronic interaction model in the CORSIKA simulation code [19] (these LOFAR result are also valid

for AERA due to the similarities of the implementation of GDAS and $X_{\max}$ reconstruction methods). An additional systematic uncertainty on the width and mean of the $X_{\max}$ distribution at a certain energy arises from the systematic uncertainty in the energy scale [44]. These effects, shown in Fig. 9, are all relatively small compared to the uncertainty from the $X_{\max}$ reconstruction itself.

Finally, we investigate any possible residual bias remaining in the data set. We check the mean of the $X_{\max}$ distribution as a function of geometry-sensitive parameters such as the shower core position and the arrival direction, which by themselves should not cause any trends in the mean $X_{\max}$ if there is no residual bias. Because the number of showers for some energy bins is rather limited we combine all showers regardless of energy and correct for the trend in energy. We define $Y_{\max}$ as the depth of the shower maximum where the elongation rate, the natural increase of the average $X_{\max}$ as a function of energy, and change in $X_{\max}$ from composition changes with energy has been corrected by subtracting the mean $X_{\max}$ of the showers in the respective energy bin $\langle X_{\max}^{\Delta E} \rangle$ and normalized to the all-data mean $\langle X_{\max} \rangle$:

$$Y_{\max} \equiv X_{\max} - (\langle X_{\max} \rangle_{\Delta E} - \langle X_{\max} \rangle). \qquad (7)$$

This now normalizes all values to roughly the average energy of the set of AERA showers and any residual trends in $Y_{\max}$ with geometry parameters can be investigated on the full set of data.

Fig. 11 shows the effect as a function of the cosine of the shower zenith angle θ. We bin the $Y_{\max}$ data in equally-sized bins and fit a line to the mean values of the bins.
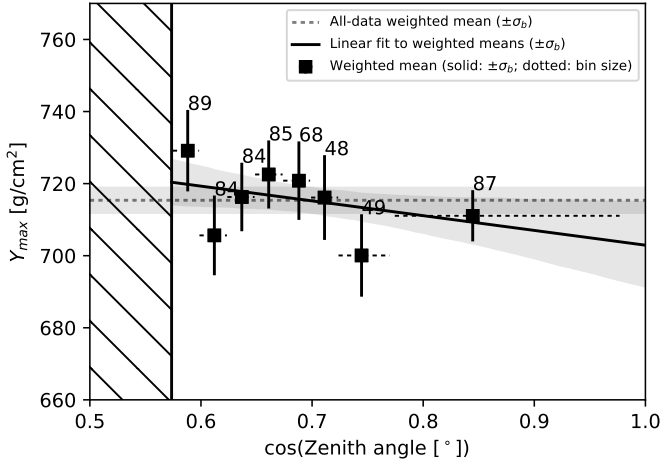
FIG. 11. Relation between $Y_{\max}$ [Eq. (7)] and the cosine of the zenith angle. The mean of $Y_{\max}$ is shown in equally-spaced bins, or merged bins if containing less than 40 showers (black squares). The number of events per bin is quoted next to each bin. The solid-line error bars show the uncertainties on the means, determined with bootstrap resampling. The dashed-line bars indicate the extent of each bin. Also shown are the mean of the entire data set (dashed line with 1σ-confidence band) and a linear fit to the mean values (solid line with 1σ-confidence band).
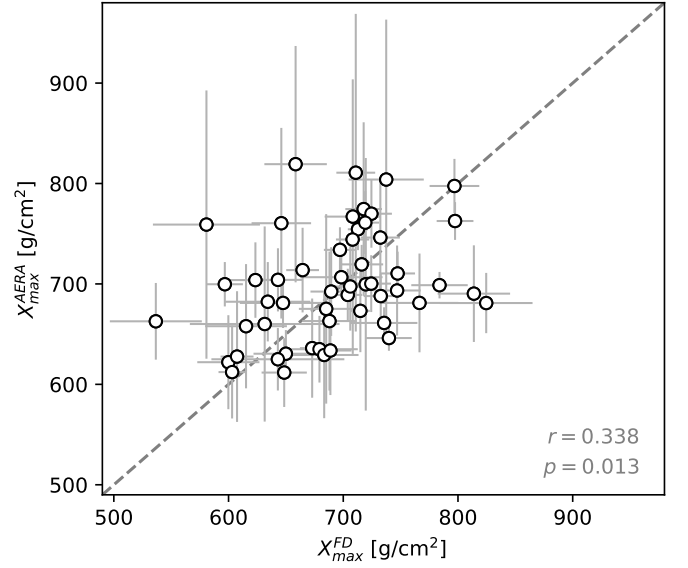

FIG. 12. Comparison of $X_{\max}$ for 53 showers measured with both FD and AERA. A diagonal (dashed gray line) is plotted to guide the eye. Also shown is the Pearson correlation coefficient r of this data and the corresponding p-value (the probability of obtaining an r from uncorrelated data that is at least as high).

The resulting linear trend (solid line) is shown to be compatible with zero slope within the 1σ uncertainty band (shaded region) and hence shows no indication of a systematic bias. Possible trends in the azimuth angle ϕ, the *geomagnetic angle* α (the angle between shower arrival direction and the geomagnetic field, which determines the strength of the geomagnetic emission), and shower core position are also investigated and show similarly small trends compatible with zero slope. Nonetheless, a possible residual bias within these uncertainties can not be excluded. Hence, for each of these geometry parameters we evaluate the effect these possible trends would have on the shower $X_{\max}$ values and calculate the magnitude of these possible residual biases in each of the energy bins and for each of the geometry parameters. This procedure is further described in Appendix B.

These parameters are heavily correlated, so their contributions are not added in quadrature, but instead, the extrema are used. This then results in a lower and upper limit on the possible $\langle X_{\max} \rangle$ systematic bias of between -6.8 and $+6.6\,\mathrm{g\,cm^{-2}}$, varying slightly depending on energy (see green bars in Fig. 9 and tabulated values in Table III). It should be noted that the constraints on these uncertainties are governed by the statistical uncertainty given by the number of showers we have available in this check. The possible systematic biases are well within the statistical uncertainties of $\langle X_{\max} \rangle$, so there is no hint that this is a significant bias and thus it should be considered an upper limit on the possible geometry-dependent bias.

It is possible we overestimate our total systematic uncertainty when adding the possible residual bias in

quadrature due to correlation with the previously determined uncertainties. Hence, we use the independent $X_{\max}$ reconstruction of the fluorescence telescopes, that is available for 53 air showers in our data set, to obtain an additional and independent estimation on the total systematic uncertainty. The FD data has been prepared as in [40] and is shown against the radio reconstruction of $X_{\max}$ in Fig. 12. Fig. 13 shows the distribution of the difference between the two reconstructions to be compatible with zero within $-3.9 \pm 11.2\,\mathrm{g\,cm^{-2}}$ for the 53 showers with energies predominately between $10^{17.5}$ and 10^{18} eV. Taking into account the systematic uncertainty on the FD $X_{\max}$ reconstruction itself for these energies (roughly $\pm 10\,\mathrm{g\,cm^{-2}}$) [40] and summing the lower and upper limit in quadrature with the FD uncertainty, results in systematic uncertainty limits of -18.1 to $+12.4\,\mathrm{g\,cm^{-2}}$ on $X_{\max}$ for these events, respectively. This estimate for the upper limit of the total systematic uncertainty matches closely to the values for the total systematic uncertainty on $\langle X_{\max} \rangle$ of Fig. 9 (on average -15.6 and $+11.2\,\mathrm{g\,cm^{-2}}$, as calculated for the energies of those 53 events). The combination of these two independent estimations of systematic uncertainties provides further support that our systematic uncertainties are well-understood and that all significant effects have been accounted for.

Furthermore, the compatibility of the direct event-to-event comparison of the two independent methods hints at the robustness of our understanding of EM cascades in air showers and its implementation in simulations. This is especially important in the context of $X_{\max}$ measurements using other aspects of the shower,
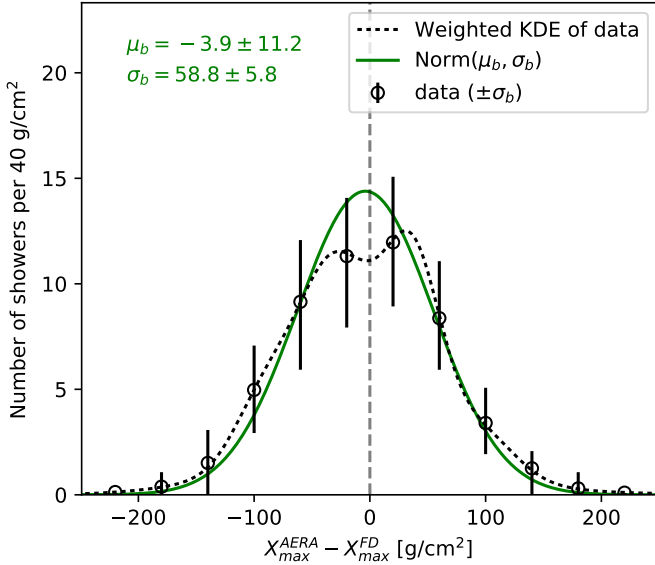
FIG. 13. Results of the comparison of $X_{\max}$ for 53 showers measured with both FD and AERA. Plotted is the weighted KDE (black dashed curve) of the event-to-event differences in $X_{\max}$ (sum of 53 Gaussian distributions with the individual differences as means and combined AERA and FD uncertainty $\delta = (\delta^2_{X^{\mathrm{AERA}}_{\max}} + \delta^2_{X^{\mathrm{FD}}_{\max}})^{0.5}$ as widths). The black markers show the spread on the KDE, evaluated at intervals of $40\,\mathrm{g\,cm^{-2}}$, obtained by repeatedly taking $N = 53$ samples from the KDE. The calculated weighted mean μ_b and width σ_b of the differences are annotated in the figure (uncertainties are calculated by bootstrap resampling where we repeatedly sample 75% of events). For comparison, the Gaussian distribution corresponding to μ_b and σ_b is plotted as solid green curve. Note that the combined resolution of FD and AERA ($53.3 \pm 5.7\,\mathrm{g\,cm^{-2}}$, as calculated from the $X_{\max}$ uncertainties of the 53 events) can account for the spread of the difference.

such as the muonic component [45], which is arguably less well-understood as suggested by the measurements of a significant muon deficit in simulations [46]. Our new constraints between the radio and fluorescence $X_{\max}$ scales might provide new hints in future studies.

V. RESOLUTION

In Fig. 14 we show the uncertainty on $X_{\max}$ as a function of shower energy, as determined with our method, for the final bias-free selection of 594 showers (see Sec. IV). We find that the median resolution in $X_{\max}$ shows a clear relation with shower energy, reaching a resolution of better than $15\,\mathrm{g\,cm^{-2}}$ in the highest energy bin. We parametrize the resolution as

$$\delta_{X_{\max}} = a \cdot \sqrt{\frac{10^{18}\mathrm{eV}}{E}} \oplus b \cdot \frac{10^{18}\mathrm{eV}}{E} \oplus c, \qquad (8)$$

inspired by the energy resolution of electromagnetic calorimeters [47], but also functioning as a generic expansion in terms of energy. Here, $a = 14.0 \pm 6.8\,\mathrm{g\,cm^{-2}}$,

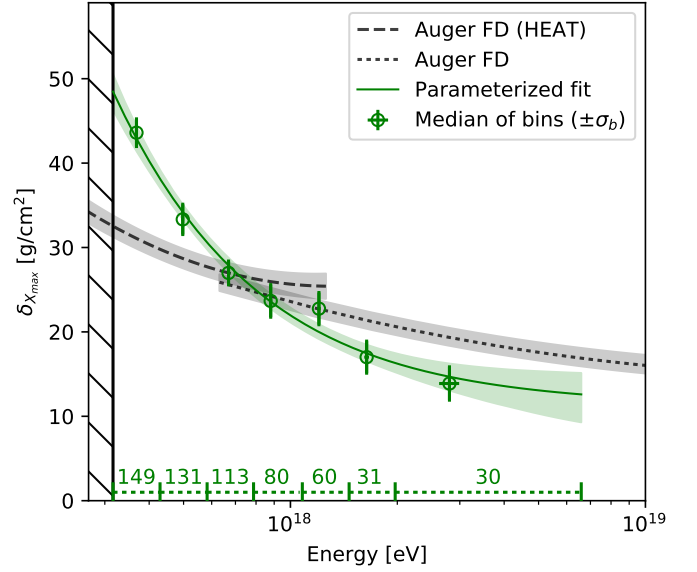FIG. 14. Resolution of the $X_{\max}$ reconstruction method, $\delta_{X_{\max}}$, as a function of energy in units of column density. Shown per energy bin are the median values of the uncertainties on $X_{\max}$ (circles with uncertainties σ_b from bootstrap resampling) for all showers in the bias-free sample (Table I) and a parametrized fit [Eq. (8)] of the resolution in $X_{\max}$ (solid line with 1σ-confidence bands). Also shown are the resolutions achieved by the Auger fluorescence telescopes [40]. The black hatched region at low energy indicates the cut on energy applied earlier. The extent of each energy bin, including the number of showers per bin, is inset at the bottom of the figure.

$b = 12.7 \pm 2.5\,\mathrm{g\,cm^{-2}}$, and $c = 11.2 \pm 4.7\,\mathrm{g\,cm^{-2}}$ are fitted free parameters and $\oplus$ indicates the quadratic sum. The constant term c provides an indication of the resolution that might potentially be obtained for AERA with this method at the highest energies (given this parametrization). The change in resolution of $X_{\max}$ is dominated by the uncertainty on the measured radio signals and hence becomes less accurate at lower energy. Comparing our resolution to the resolution achieved by FD, we achieve similar values at the highest energies where the FD reaches $15\,\mathrm{g\,cm^{-2}}$ [40]. Furthermore, our method remains competitive down to lower energies where, for example at $E = 10^{17.8}\,\mathrm{eV}$ the FD achieves the same resolution of $25\,\mathrm{g\,cm^{-2}}$. The most recent results by the LOFAR radio array, where a similar simulation-fitting method is used to determine $X_{\max}$, report an average resolution of $19\,\mathrm{g\,cm^{-2}}$ between $10^{16.8}$ and $10^{18.3}\,\mathrm{eV}$ [48]. Despite the much denser antenna spacing of LOFAR, AERA achieves similar resolutions considering the respective energy regimes to which the two experiments are sensitive.

We note that up till now it has been common to quote a single resolution value for $X_{\max}$ reconstruction methods for radio experiments, mainly because of a limited number of measured showers being available. Here we show the resolution in $X_{\max}$ depends strongly on the shower
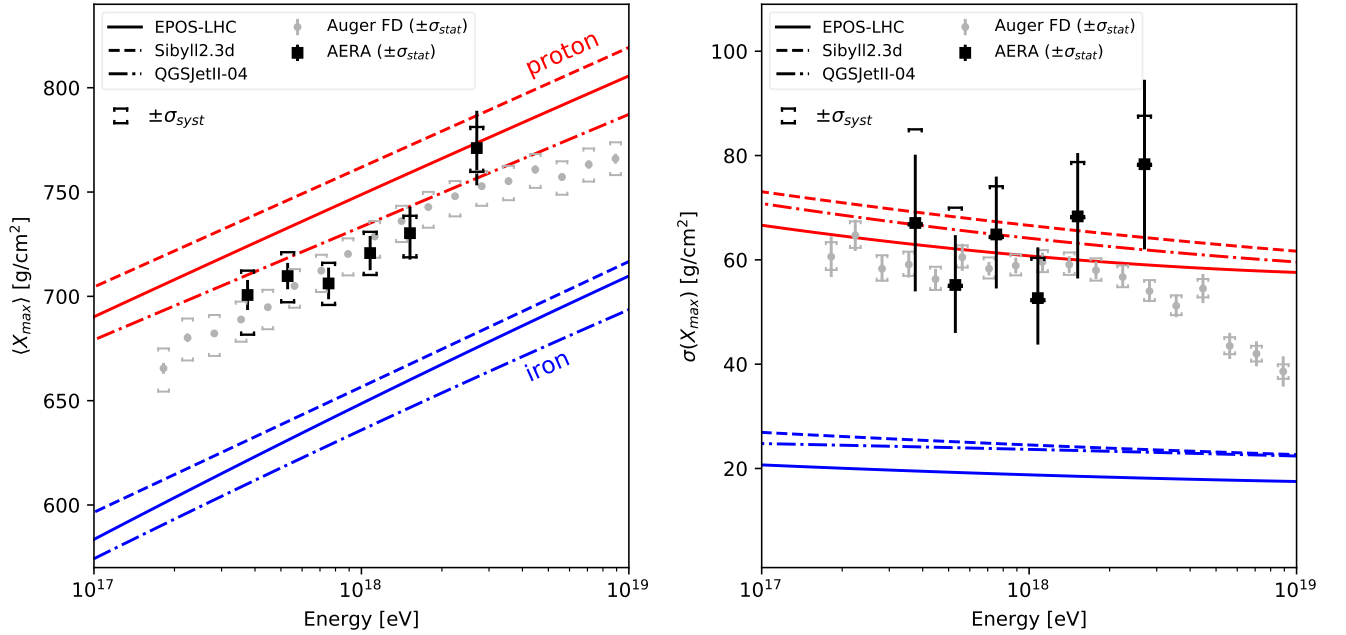
FIG. 15. Mean (left) and (resolution-subtracted) width (right) of the X_{max} distribution as measured by AERA in this work (black). The results are compared to predictions from CONEX air-shower simulations for three hadronic interaction models (lines) for proton (red) and iron (blue) mass compositions [31, 49–51] and compared to measurements by the FD (gray) [51]. The statistical uncertainties on the mean and width of the experimental results are plotted as error bars and the systematic uncertainties are shown with caps.

energy, driven primarily by the strength of radio signals measured in the antennas. Hence, the resolution is a function of detector sensitivity, shower energy, and thus heavily depends on the shower selection criteria. As such, any direct comparison of methods is less straightforward if obtained at sufficiently dissimilar detectors.

VI. THE X_{max} MOMENTS AND THE DISTRIBUTION OF X_{max}

From the X_{max} distribution, for each of our six energy bins, we now also calculate the first two moments of the distribution, the mean $\langle X_{max} \rangle$ and the width $\sigma(X_{max})$. To obtain the latter we first subtract in quadrature the width caused by the method uncertainty, such that only the width caused by shower-to-shower fluctuations $\sigma(X_{max})$ remains. The method uncertainty cannot simply be characterized by a single value since the uncertainties on X_{max} for our air showers do not necessarily follow a Gaussian distribution. A bootstrap resampling procedure is applied for this reason and with this we then also calculate the uncertainty on $\sigma(X_{max})$. This procedure is further described in Appendix C. The resulting mean and width of the true X_{max} distribution are shown in Fig. 15, where we also compare this to the results from the FD (gray) and theoretical predictions of three different hadronic interaction models for a mass composition of just protons (red) or just iron nuclei (blue). The systematic uncertainties determined in the previous section

are shown with capped markers. Table IV in Appendix D lists the values for the two moments of the distributions for the six energy bins, together with their statistical and systematic uncertainties.

With these AERA results we show good agreement between the Auger radio and fluorescence measurements of $\langle X_{max} \rangle$, both pointing towards a (mixed)-light composition of cosmic rays at around $E = 10^{17.5}$ eV. Note that the two measurements share the systematic uncertainty on the energy scale, which is constructed from calibration of the SD energy to the FD energy scale [44]. Taking this contribution out, reduces both systematic uncertainty bands by about $3 \, \mathrm{g \, cm^{-2}}$. Secondly, the determination of the systematic uncertainties due to the reconstruction method for AERA X_{max} data depends on the assumed composition. We have conservatively taken the most pessimistic mass composition scenario for our method. If we were to assume a (mixed) light composition, as the FD reports, then the composition-dependent AERA systematic uncertainty from the reconstruction method and the acceptance calculation, combined, would be reduced to only a small contribution ($\sigma_{\mathrm{stat.}}^{\mathrm{low}} = 0 \, \mathrm{g \, cm^{-2}}$ at all energies, roughly $\sigma_{\mathrm{stat.}}^{\mathrm{up}} = 5 \, \mathrm{g \, cm^{-2}}$ for all but the highest energy bin, and roughly $\sigma_{\mathrm{stat.}}^{\mathrm{up}} = 7 \, \mathrm{g \, cm^{-2}}$ for the highest bin)). This happens because the AERA systematic uncertainties originate primarily from systematic uncertainties on the reconstruction of the very deepest or very shallowest X_{max} values, which would not significantly impact the average X_{max} for a (mixed) light composition. In that case, the total systematic uncertainty on $\langle X_{max} \rangle$
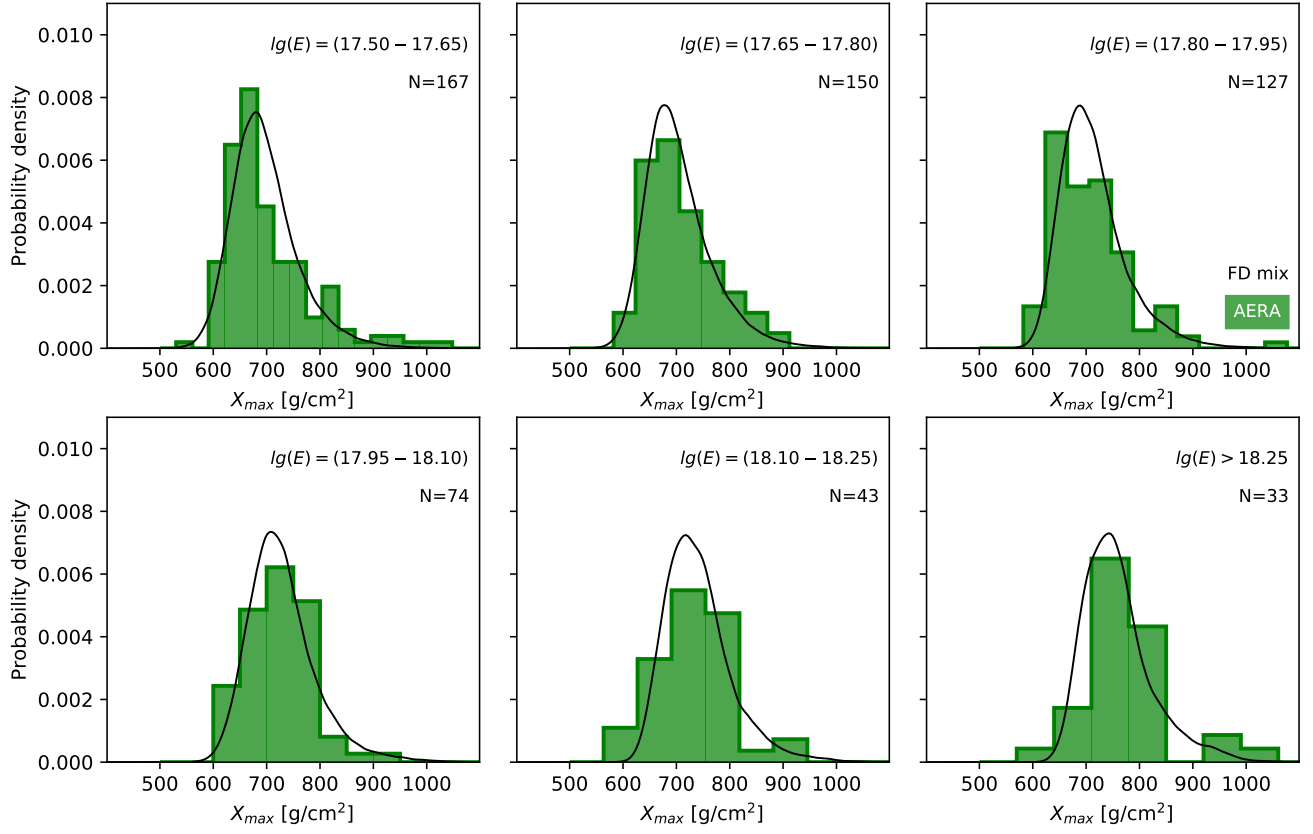
FIG. 16. Distribution of $X_{\max}$ measured with AERA (green) for six energy bins. These distributions still include the effects of detector resolution, bias, and acceptance. The distributions are compared to the mixed-mass composition as measured by Auger FD [40] (black), which has been convolved with the detector effects of AERA to allow for direct comparison to the AERA distribution (see main text). Energy ranges and number of showers are annotated in the figures.

would be just below $\pm 10\,\mathrm{g\,cm^{-2}}$ for all energies.

The AERA results of the second moment of $X_{\max}$, shown on the right side of Fig 15 also shows compatibility with the FD results, but have limited resolving power because of the smaller number of showers in comparison to the FD measurements. In the highest AERA energy bin, $\sigma(X_{\max})$ is somewhat higher than for the FD. Note that this bin contains just 33 showers, so a single extreme event in the tail of the $X_{\max}$ distribution could result in the observed upwards fluctuation (consequently, the same effect is seen in the first moment for this energy bin). Hence, this single fluctuation is not considered a particularly significant deviation from the FD values within the shown statistical uncertainties.

In Fig. 16 we show the full distributions of the AERA-reconstructed $X_{\max}$ values for the bias-free set of 594 showers (Table I), split again into six energy bins. For comparison, we superimpose the $X_{\max}$ distributions for the mixed-mass composition as determined by the Auger FD measurements (black) [40] which has been convolved with the acceptance, biases, and uncertainties of the AERA $X_{\max}$ values and the uncertainty on the FD composition. In this way, a direct comparisons between the FD and AERA $X_{\max}$ distribution can be made.

We quantify the compatibility between the FD and AERA $X_{\max}$ distributions by calculating the probability we would draw the AERA event sample from the FD distribution, including the known acceptance, uncertainties, and biases from AERA, the uncertainties from the FD composition measurement, and the systematic uncertainties on $X_{\max}$ between the FD and AERA. The FD $X_{\max}$ distribution is here represented by Gumbel distributions [41, 42] fitted to the FD $X_{\max}$ distributions, accounting for detector resolution and acceptance [40]. This allows us to easily sample from the distribution and add AERA measurement effects, such that we can compare quantities between FD and AERA on the same level.

For each AERA energy bin we repeatedly ($N = 1000$) generate FD $X_{\max}$ distribution instances from the Gumbel parametrization of the FD composition, evaluated at the energies of the AERA events in that bin. For each instance, we vary the composition within its statistical uncertainties (using many instances of the composition fit to the FD composition [40]). Next, we draw, from each distribution, a set of $X_{\max}$ values, with the same number of events as we have for AERA for that energy bin. When drawing values we take into account the AERA acceptance (see e.g., Fig. 8). Each drawn $X_{\max}$ value we

shift by its measurement uncertainty and its reconstruction bias. Both quantities are obtained from a parameterization of the difference between our reconstructed X_{max} and the true MC X_{max} for all our CORSIKA simulations ($N_{sim} = 27 \times 594$) as a function of shower energy and MC X_{max}. This parametrization contains both the average and spread of the measurement uncertainties and bias, which are then used to draw shifts randomly. With this procedure, we obtain 1000 'mock data sets', drawn from the FD distribution, that include the main detection and reconstruction effects of AERA. These now represent X_{max} data set instances that AERA would have measured assuming the FD composition. We can now start to compare these to the actual AERA X_{max} data set to check the compatibility of the AERA and FD distribution.

To quantify the compatibility we use the *Kolmogorov-Smirnov* (KS) and *Anderson-Darling* (AD) tests (see e.g., [52]), similarly to the compatibility tests of the X_{max} distributions of the Auger FD and Telescope Array FD [53]. These tests are commonly used to test if a data sample follows a specified distribution. The KS test is particularly suited to test for compatibility in the region around the peak of the distribution, while the AD test also provides sensitivity to the tails of the distribution. Together they are a good measure for the agreement for the overall shape of the distribution. We calculate the KS test statistic D as

$$D = \max_{1 \leq i \leq N} \left(F(X_i) - \frac{i-1}{N}, \frac{i}{N} - F(X_i) \right), \quad (9)$$

and the AD test statistic A^2 as

$$A^2 = -N - S, \quad (10)$$
$$S = \sum_{i=1}^{N} \frac{2i-1}{N} \left[\ln F(X_i) + \ln \left(1 - F(X_{N+1-i}) \right) \right],$$

where X_i are the (ordered) data points in a sample, N is the number of samples, and F is the cumulative distribution function of the distribution being tested.

The distribution that we test our samples against we construct as the Gaussian KDE of the 1000 FD-drawn samples, such that we have a probability density function from which we can obtain the cumulative distribution function F. We then calculate D and A^2 for each of the individual FD-drawn samples. This provides the range of expected AD and KS test statistics given the sampling effects of AERA measurements. The resulting test statistics are shown in Fig. 17 (gray histograms). Next, we calculate the test statistics of the AERA data itself and evaluate where it falls within the test statistic distribution (green lines in the same figure). From this, we obtain the probability p of finding a test statistic value larger than the value for the AERA data, i.e., the chance that a sample taken from the distribution under examination is as compatible as the AERA data. The p values are shown in Fig. 17 and listed in Table II. We

take $p < 0.05$ as the threshold to reject the null hypothesis of compatibility. Before interpreting the probabilities, we also have to account for systematic uncertainties. We calculate the effect on the KS and AD test statistics for the AERA data sample for a general shift of the X_{max} distributions allowed within the systematic uncertainties of $\langle X_{max} \rangle$. The systematic uncertainties between AERA and FD consist of the contribution of the FD measurements (roughly $\pm 10 \, \mathrm{g \, cm^{-2}}$) [40] and the AERA contributions that were not included in the earlier modelled bias correction when generating F, namely the effects of the model for the atmosphere and the hadronic interaction model used in our CORSIKA simulations ($\pm 5.5 \, \mathrm{g \, cm^{-2}}$ in total, see also Fig 9). The upper and lower values obtained for the test statistics and the corresponding p values are shown in Fig. 17 (green bands).

For the KS test, we find that the AERA data is compatible with the Auger FD composition (FD mix) within the uncertainties for all energy bins, but note that for the third energy bin this requires a small shift allowed within systematic uncertainties. The AD test, similarly, finds compatibility for all energy bins, but requires a shift within systematic uncertainties for the first and third energy bins. We investigate if the required shifts agree with each other, i.e., that compatibility also holds for all energy bins at the same time. For this, we calculate the KS and AD test statistics for the AERA data sample for a range of shifts of X_{max}. For the simplest scenario of a constant shift at all energies, the best overall match for all energy bins is obtained with a general shift of $\Delta X_{max}^{best} = X_{max}^{AERA} - X_{max}^{FD} = -5.5 \pm 0.7 \, \mathrm{g \, cm^{-2}}$ which falls well within the systematic uncertainties. The uncertainty of $0.7 \, \mathrm{g \, cm^{-2}}$ here shows the range of a constant shift where all energy bins show compatibility for both KS and AD test (for the $p \geq 0.05$ threshold). The p values for this shift are listed in the central columns of Table II and show that for both tests $p > 0.05$, i.e., compatibility between AERA and FD X_{max} measurements. Furthermore, this shift is in agreement with the shift of $-3.9 \pm 11.2 \, \mathrm{g \, cm^{-2}}$ obtained for the event-by-event comparison of hybrid events (Fig 13).

We note that the systematic shift between AERA and FD does not need to be a simple constant, but might depend on energy. Hence, we also calculate the p values for separate shifts per energy bin that lead to the best match between AERA and FD (i.e., highest p). The values for p and corresponding shifts (calculated for KS and AD tests separately) are shown in the column on the right in Table II. We note that the shifts show no significant trend with energy, suggesting that there is no strong dependence on energy in the systematic uncertainties between AERA and FD. Furthermore, the KS and AD tests agree on the obtained shifts, indicating that both the central part and the tails of the X_{max} distribution, respectively, favour such a shift. The uncertainties on the shifts give a good indication that the KS and AD tests are able to constrain the cosmic-ray composition with the AERA measurements.
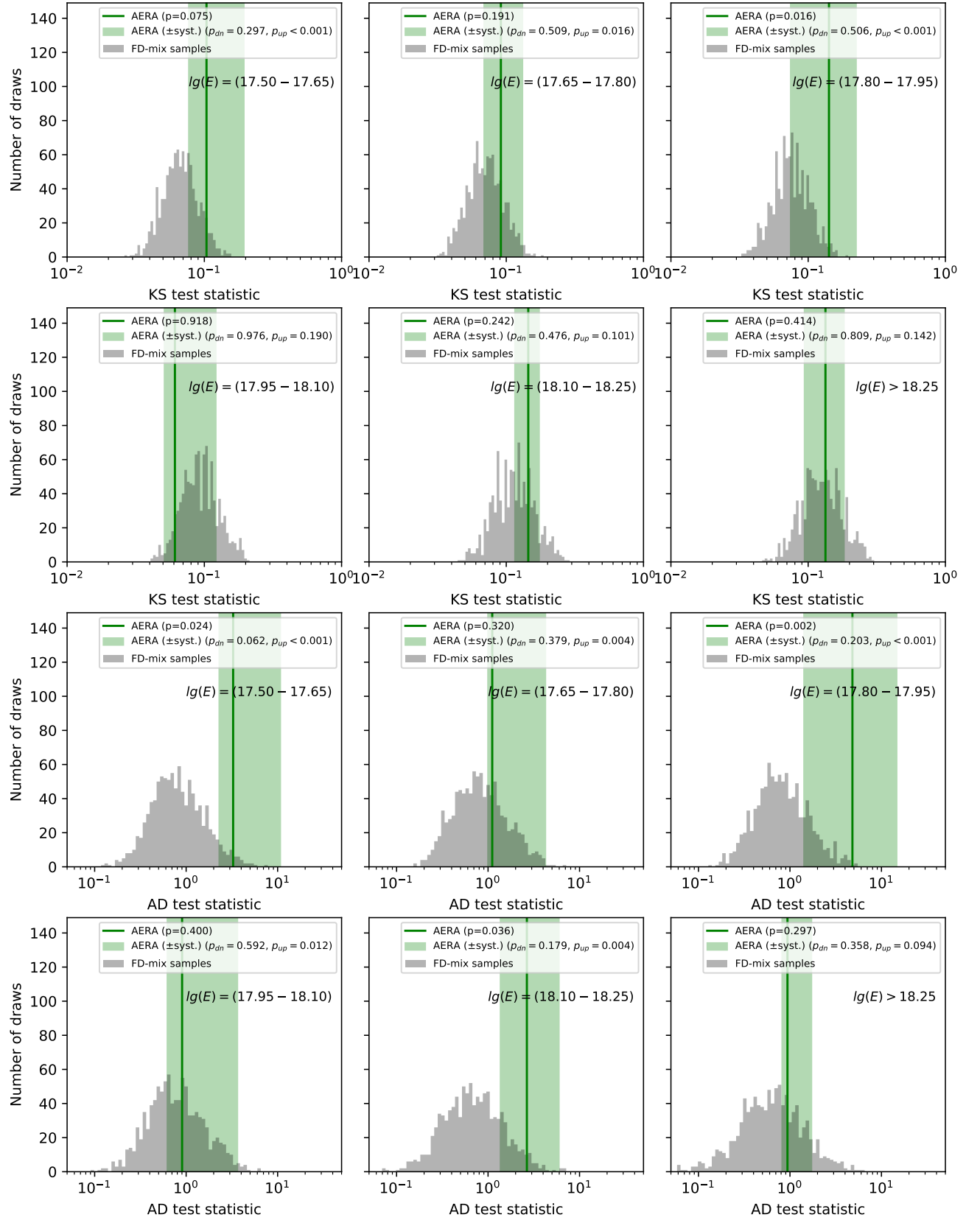
FIG. 17. Compatibility test of the AERA data and the composition as measured by the Auger FD. Results are shown for six energy bins (values shown in each panel). The top six panels show the distribution of the Kolmogorov-Smirnov (KS) test statistic (gray histograms) for 1000 $X_{\max}$ samples generated from the FD composition as would be measured by AERA (i.e., including the effects of the FD composition uncertainties and AERA reconstruction bias, resolution, and acceptance). The green line in each panel shows the KS test statistic for the AERA data sample (with systematic uncertainty band). The probabilities for compatibility are quoted in the legend and listed in Table II. The bottom six panels show the same procedure for the Anderson-Darling (AD) test.

TABLE II. Probabilities for the AERA $X_{\max}$ distribution to be drawn from the FD composition, evaluated with the Kolmogorov-Smirnov (KS) and Anderson-Darling (AD) tests, as described in Sec. VI). Probabilities are quoted per energy bin, listing the values for three scenarios: no shift $\Delta X_{\max}$ between the AERA and FD $X_{\max}$ distributions (left), the best-matching overall constant shift of $\Delta X_{\max}^{\text{best}} = X_{\max}^{\text{AERA}} - X_{\max}^{\text{FD}} = -5.5\,\text{g\,cm}^{-2}$ (center), and best-matching shift for each energy bin and test statistic separately (right). The corresponding shifts are also listed including the range where the test statistic results in $p \geq 0.05$.

lg(E[eV])	no shift		constant shift		variable shift			
	KS	AD	KS	AD	KS		AD	
range	p value	p value	p value	p value	shift [g cm^{-2}]	p value	shift [g cm^{-2}]	p value
[17.50, 17.65)	0.075	0.024	0.278	0.062	$4.5^{+10.2}_{-5.5}$	0.278	$5.1^{+2.5}_{-1.0}$	0.062
[17.65, 17.80)	0.191	0.320	0.051	0.071	$-5.0^{+11.0}_{-5.8}$	0.509	$-2.1^{+8.2}_{-7.7}$	0.365
[17.80, 17.95)	0.016	0.002	0.157	0.062	$9.1^{+12.1}_{-6.0}$	0.506	$13.1^{+7.0}_{-8.3}$	0.203
[17.95, 18.10)	0.918	0.400	0.685	0.573	$3.0^{+13.4}_{-21.5}$	0.974	$5.0^{+12.7}_{-13.6}$	0.566
[18.10, 18.25)	0.242	0.036	0.476	0.111	$10.5^{+19.3}_{-26.5}$	0.476	$16.0^{+12.6}_{-14.7}$	0.179
[18.25, ∞)	0.414	0.297	0.200	0.172	$-10.5^{+30.7}_{-18.4}$	0.809	$-6.0^{+19.4}_{-15.4}$	0.352

In conclusion, the AERA $X_{\max}$ distribution provides further support, beyond just the $X_{\max}$ moments, for compatibility with the FD $X_{\max}$ measurements and suggests a similar general shift between the AERA and FD distributions as for the event-by-event comparison in Fig 13 (a shift of about $-4\,\text{g\,cm}^{-2}$). Furthermore, the compatibility indicates that the uncertainties, biases and acceptance of the AERA measurements are well understood.

compatibility with the composition as previously measured by the FD. In addition, the compatibility of the overall shape of the $X_{\max}$ distributions between AERA and the FD provides further support beyond the two central moments for the mixed-light composition as previously measured by the FD. Discussions on the comparison of the $X_{\max}$ moments to other experiments is available in an accompanying publication [21].

VII. CONCLUSIONS

In this work we show the results of the measurement of the distribution of depth of the shower maximum for air showers measured with the Auger Engineering Radio Array at the Pierre Auger Observatory. We have presented the method used to reconstruct the depth of the shower maximum by comparing measured radio signals to signals from dedicated sets of CORSIKA/CoREAS air-shower simulations. We show that the resolution of our method is competitive with established techniques to determine $X_{\max}$. We have selected a set of air showers with minimal selection bias and have quantified any remaining acceptance bias. Furthermore, a detailed study of systematic uncertainties has been conducted accounting for the effects of the reconstruction method, the use of simulation codes, atmospheric models, the energy scale, and possible geometry-dependent residual bias. The total estimated systematic uncertainties on the mean of the $X_{\max}$ distribution has been shown to be compatible with an event-by-event comparison of 53 showers measured by both the Auger fluorescence and radio detectors, indicating a good understanding of the systematic uncertainties in the AERA measurements. In addition, this direct comparison sets a limit on the systematic shift between the AERA and FD $X_{\max}$ scale of $-3.9 \pm 11.2\,\text{g\,cm}^{-2}$, providing new constraints on our understanding of shower physics.

The calculated moments of the $X_{\max}$ distribution show

Appendix A: Calculation of Systematic Uncertainties

1. Calculation of the Systematic Uncertainty from the Event Selection

The acceptance $A(X_{\max})$ for a particular measured air shower was determined from evaluating reconstructability of each of the 27 air-shower simulations created for that measured shower. The $X_{\max}$ values for these showers roughly cover, by design, the range between 500 and $1100\,\mathrm{g\,cm^{-2}}$ such that an interpolated acceptance-$X_{\max}$ function can be constructed for each shower. The effect the acceptance would have on measuring an $X_{\max}$ distribution is quantified by evaluating the two extreme cases of a mass composition described by a $X_{\max}$ Gumbel distribution for just protons $G^{\mathrm{p}}(X_{\max})$, just iron nuclei $G^{\mathrm{Fe}}(X_{\max})$, a mix 50:50 mix of the two $G^{50:50}(X_{\max})$, and the composition as measured by the Auger FD $G^{\mathrm{AugerMix}}(X_{\max})$. The effect on the mean of such an $X_{\max}$ distribution is then calculated and compared to the unaffected Gumbel distribution. The average effect over all events in a particular energy bin is then calculated in order to estimate the systematic shift this might cause on the distribution of measured $X_{\max}$ values at these energies. Since the measured composition is not *a priori* known the least favourable composition C (i.e., whichever has the highest bias) is assumed and this is taken as upper and lower limit on the systematic uncertainty on $\langle X_{\max} \rangle$:

$$
\begin{aligned}
\langle X_{\max} \rangle^A_{\mathrm{syst,low}} = \min_{\mathrm{C}} [\langle \\
\left\langle A_{\mathrm{event}}(X_{\max}) \cdot G^{\mathrm{C}}_{\mathrm{event}}(X_{\max}) \right\rangle_{X_{\max}} \\
- \left\langle G^{\mathrm{C}}_{\mathrm{event}}(X_{\max}) \right\rangle_{X_{\max}} \\
\rangle_{\mathrm{events}}],
\end{aligned} \quad (A1)
$$

$$
\begin{aligned}
\langle X_{\max} \rangle^A_{\mathrm{syst,up}} = \max_{\mathrm{C}} [\langle \\
\left\langle A_{\mathrm{event}}(X_{\max}) \cdot G^{\mathrm{C}}_{\mathrm{event}}(X_{\max}) \right\rangle_{X_{\max}} \\
- \left\langle G^{\mathrm{C}}_{\mathrm{event}}(X_{\max}) \right\rangle_{X_{\max}} \\
\rangle_{\mathrm{events}}].
\end{aligned} \quad (A2)
$$

The same procedure is performed for the width of the $X_{\max}$ distribution instead of the mean in order to estimate the systematic uncertainty on $\sigma(X_{\max})$. The results, as a function of energy, for both moments of the $X_{\max}$ distribution are shown in Fig. 9.

2. Calculation of the Systematic Uncertainty from the X_{max} Reconstruction Method

The systematic effect from any X_{max} reconstruction bias in our method on the mean of the true X_{max} distribution $\langle X_{\mathrm{max}} \rangle$ and the spread $\sigma(X_{\mathrm{max}})$ are calculated by evaluating the effect on the Gumbel distribution for a pure proton mass composition, pure iron mass composition, and a 50:50 mix of the two. This is done for the same energy bins as for the systematic uncertainty calculation on the acceptance.

The first step is to weigh down the simulations in our simulation set that are rare according to the true X_{max} distributions. These weights are ideally set by the actual distribution in nature, but are *a priori* unknown. What can be assumed, however, is that the composition lies between a pure proton and pure iron mass composition. An upper limit on the systematic uncertainty on X_{max} can then be defined conservatively as the maximum systematic uncertainty determined for the three mass compositions cases. In the same way as was done for the systematic uncertainty on the acceptance. This upper and lower limits will be used as the estimation of the systematic uncertainty on the two moments of the X_{max} distribution.

The weights w for the simulations with $X_{\mathrm{max}}^{\mathrm{MC}}$ are then defined for a particular composition described by a Gumbel distribution G (or sum of Gumbel distributions for a mixed composition):

$$w(X_{\mathrm{max}}^{\mathrm{MC}}) = \frac{\mathrm{PDF}(X_{\mathrm{max}}^{\mathrm{Gumb}})}{\mathrm{PDF}(X_{\mathrm{max}}^{\mathrm{MC}})}, \tag{A3}$$

where the numerator is the standard Gumbel probability distribution for X_{max} for a particular composition of cosmic rays. The denominator is a Gaussian KDE of the simulated X_{max} values. The latter functions as the probability density function of the simulated values.

This then allows us to calculate the mean of the X_{max} distribution from the simulations, under the assumption of a certain composition. The mean of all $X_{\mathrm{max}}^{\mathrm{MC}}$ (weighted to the Gumbel distribution),

$$\langle X_{\mathrm{max}}^{\mathrm{MC}} \rangle_{\mathrm{Gumb}} = \frac{\sum_{\mathrm{sim}} \left(X_{\mathrm{max}}^{\mathrm{MC}} \right)_{\mathrm{sim}} \cdot w_{\mathrm{sim}}}{\sum_{\mathrm{sim}} w_{\mathrm{sim}}}, \tag{A4}$$

by design, approaches the mean of the ideal Gumbel distribution, assuming sufficient number of simulations used in the KDE. For each simulation (with $X_{\mathrm{max}}^{\mathrm{MC}}$), a value for X_{max} was reconstructed for which the mean can now be calculated in the same way:

$$\langle X_{\mathrm{max}} \rangle_{\mathrm{Gumb}} = \frac{\sum_{\mathrm{sim}} \left(X_{\mathrm{max}} \right)_{\mathrm{sim}} \cdot w_{\mathrm{sim}}}{\sum_{\mathrm{sim}} w_{\mathrm{sim}}} \tag{A5}$$

$$= \langle X_{\mathrm{max}}^{\mathrm{MC}} \rangle_{\mathrm{Gumb}} + \Delta X_{\mathrm{max}}^{\mathrm{bias}}. \tag{A6}$$

This provides an estimation of the bias in $\langle X_{\mathrm{max}} \rangle$ for a particular composition C. As for the calculation of the systematic uncertainty on the acceptance, we conservatively assume the least favourable composition to obtain the systematic uncertainty on the reconstruction method

$$\langle X_{\mathrm{max}} \rangle_{\mathrm{syst,low}}^{\mathrm{method}} = \max_{C} \left[\Delta X_{\mathrm{max}}^{\mathrm{bias},C} \right] \tag{A7}$$

$$\langle X_{\mathrm{max}} \rangle_{\mathrm{syst,up}}^{\mathrm{method}} = \min_{C} \left[\Delta X_{\mathrm{max}}^{\mathrm{bias},C} \right] \tag{A8}$$

A similar calculation is performed to determine the systematic uncertainty on the width of the Gumbel distributions for the AERA values. To obtain this, the mean is replaced by a calculation of the standard deviation, such that $\sigma(X_{\mathrm{max}})_{\mathrm{syst,low}}^{\mathrm{method}}$ and $\sigma(X_{\mathrm{max}})_{\mathrm{syst,up}}^{\mathrm{method}}$ are determined. The resulting systematic uncertainty ranges are shown in Fig. 9.

Appendix B: Calculation of the possible residual bias

To calculate the effect of possible residual bias depending on geometry parameters such as shower zenith angle or core position, we investigate potential trends with X_{max}. The mean X_{max} changes with energy, so we defined Y_{max} as in Eq. (7) such that this expected dependence can be removed and any remaining residual biases can be identified for the data set as a whole.

We investigate the dependence of Y_{max} as a function of shower zenith angle θ, geomagnetic angle α, and core position in x and y coordinates (relative to the center of the Auger array). The azimuth angle ϕ has been checked for a possible sinusoidal trend, but shows no variation that is not already explained by zenith or geomagnetic angle dependencies, hence is not shown. For each of these geometry parameters, event selection might be affected by the irregular AERA antenna spacing and various antenna hardware types used in AERA, despite the acceptance cuts that were implemented (see Sec. IV). We split up the Y_{max} data set in regular bins for each of these variables and calculate the mean of Y_{max} in each of these bins. The uncertainty on Y_{max} combines the uncertainties of X_{max} and the energy dependence that was compensated for. The uncertainty on these mean values is determined by bootstrap resampling where we repeatedly sample 75% of the data and look at the variations in the mean. This procedure is done such that both the non-Gaussian distribution of Y_{max}, the uncertainties on Y_{max}, and statistical uncertainties from the limited number of showers can all be accounted for properly.

Fig. 18 shows the mean values as a function of the cosine of the zenith angle, geomagnetic angle, shower core x coordinate, and shower core y coordinate, respectively (black squares). The solid-line error bars show the uncertainties on the means from the bootstrap resampling. The dashed-line bars indicate the extent of each bin. Also shown are the mean of the entire data set (dashed line with 1σ-confidence band) and a linear fit to the mean values (solid line with 1σ-confidence band). The hatched
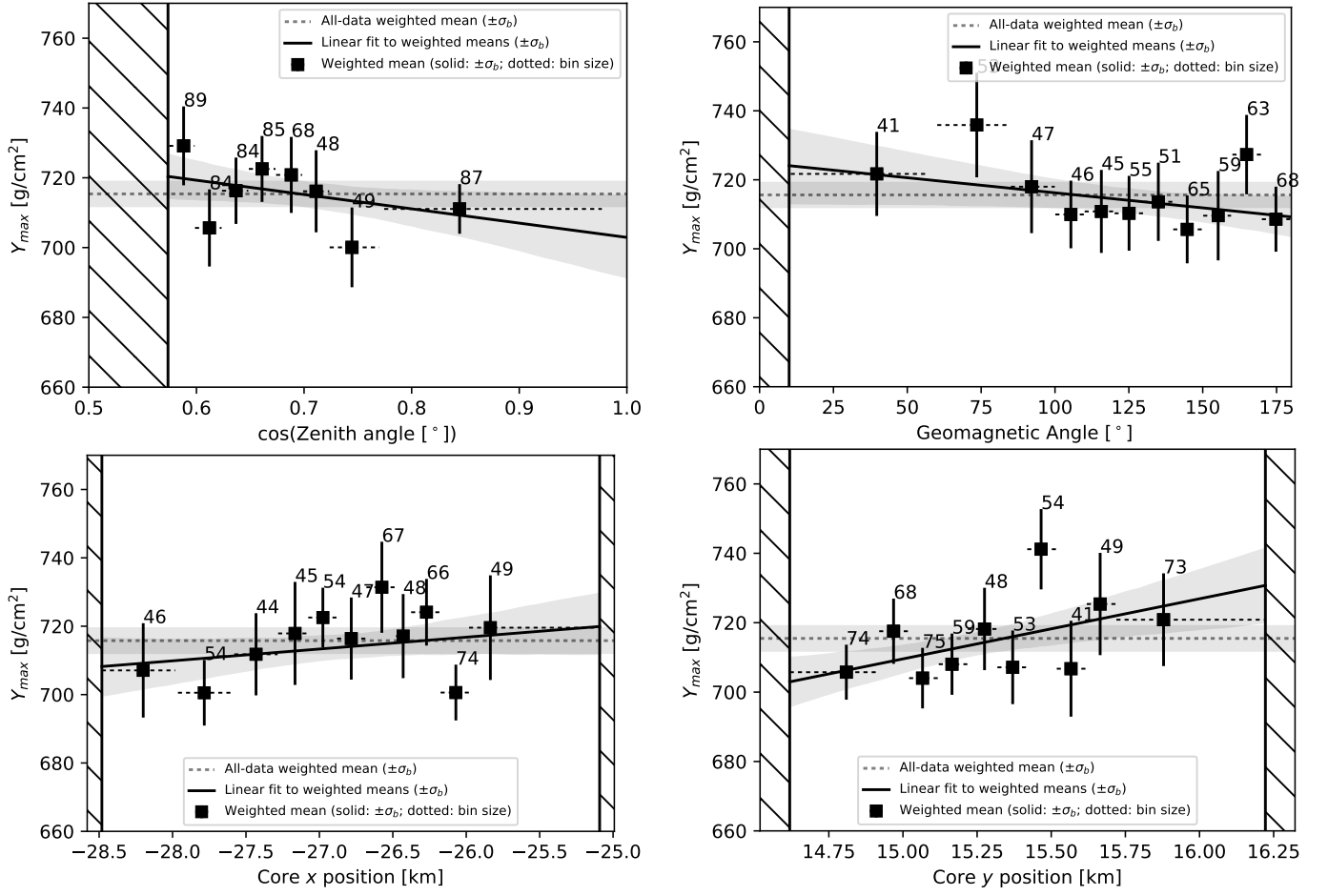
FIG. 18. Relation between $Y_{\max}$ [Eq. (7)] and the cosine of the zenith angle (top left), geomagnetic angle (top right), core position x coordinate (bottom left), and core position y coordinate (bottom right). Both core coordinates are relative to the center of the Auger array. The mean of $Y_{\max}$ is shown in equally-spaced bins, or merged bins if containing less than 40 showers (black squares). The number of events per bin is quoted next to each bin. The solid-line error bars show the uncertainties on the means, determined with bootstrap resampling. The dashed-line bars indicate the extent of each bin. Also shown are the mean of the entire data set (dashed line with 1σ-confidence band) and a linear fit to the mean values (solid line with 1σ-confidence band).

regions indicate where no data is present, either from prior cuts or physical constraints.

None of the trends show a significant deviation from the all-data mean values within their uncertainties and as such we can say that there are no significant residual biases that depend on these geometry parameters. In other words, any possible bias in $Y_{\max}$ would need to be independent of geometry, which would be difficult to envision.

This is not to say that there is no residual bias; within the fit uncertainties there is the possibility for bias to exist. Hence, next we calculate the expected possible residual bias within the statistical uncertainties of our data set. We take as reference point the values of the geometry parameters $G \subset (\cos\theta, \alpha, x, y)$ where the least bias is expected (i.e., where detector sensitivity is optimal). This will provide us with an estimate for possible bias in possibly less sensitive regimes. Using the linear fits $Y(G)$

we calculate the shift of each shower $Y_{\max}$ value under the assumption that the $Y_{\max}$ value at the expected G value $G_{\exp}$ is the true bias-free value. This expected value for zenith angle is $\theta_{\exp} = 55°$, the highest zenith angle allowed in our data set and also where the footprints are largest and antenna sensitivity is excellent for the AERA antenna types. Hence, the acceptance would arguably be least affected there and any bias in less sensitive regimes we can determine w.r.t. this value. For the geomagnetic angle we choose $\alpha_{\exp} = 180°$, where the geomagnetic radio emission is at a maximum. For the core position we pick $x_{\exp} = -26.1\,\text{km}$ and $y_{\exp} = 15.1\,\text{km}$, corresponding approximately to the center of the part of AERA with the densest antenna spacing (see Fig. 3).

This shift in $Y_{\max}$ is then given for each individual shower by:

$$\Delta Y_{\max} = Y(G) - Y(G = G_{\exp}). \tag{B1}$$

The bias for each geometry parameter G is then given by the difference of the mean $Y_{\max}$ of the showers in a certain energy bin, with and without the correction to the expected bias-free G:

$$\text{Bias}_G = \langle Y_{\max} \rangle - \langle Y_{\max} - \Delta Y_{\max} \rangle. \qquad \text{(B2)}$$

It should be noted that the biases from the geometry parameters are highly correlated quantities and as such cannot be summed in quadrature to get a total uncertainty. Hence, the extrema of the set of possible biases $\{\text{Bias}_G\}$ is used to determine an upper and lower limit on the possible residual bias:

$$\text{Bias}^{\text{up}} = \text{Max}\left[\{\text{Bias}_G\}\right], \qquad \text{(B3)}$$
$$\text{Bias}^{\text{low}} = \text{Min}\left[\{\text{Bias}_G\}\right]. \qquad \text{(B4)}$$

This then provides an estimation for the possible residual bias in $Y_{\max}$ allowed within the statistical uncertainties of the shower data set, for each of the energy bins. From the definition of $Y_{\max}$ [Eq. (7)] it follows that these $\langle Y_{\max} \rangle$ bias values apply also to $\langle X_{\max} \rangle$. The result of the $\text{Bias}^{\text{up}}(E)$ and $\text{Bias}^{\text{low}}(E)$ on $\langle X_{\max} \rangle$ are shown in Fig. 9. The possible bias does not seem to be dominated by any single effect and does not change significantly with energy. It indicates that within the statistical uncertainties with which we can constrain any bias we are potentially biasing our $X_{\max}$ values between $\pm 7\,\text{g\,cm}^{-2}$. Table III lists the contributions of the geometry parameters per energy bin. All values are well within the statistical uncertainty on $\langle X_{\max} \rangle$ itself and hence there is no hint of any significant residual bias in this analysis.

Cross-checks have been done to test that additional artificially introduced biases (e.g., adding a linear $X_{\max}$ (α) dependence) can be recovered with this procedure to a degree that the $\text{Bias}^{\text{up}}(E)$ and $\text{Bias}^{\text{low}}(E)$ indeed account for the artificial bias. Additionally, also the effect on the median $Y_{\max}$ versus the geometry parameters has been evaluated. Compared to using the mean, the median is less sensitive to the shape of the tail of a distribution (i.e., less sensitive to large outliers) and thus has an increased sensitivity to a more general shift of the distribution. Also here no significant trend was found and the allowed possible biases were similarly small.

Appendix C: Calculation of the Second Moment of the $X_{\max}$ Distribution

The true distribution of $X_{\max}$ can be estimated from the width of the AERA $X_{\max}$ distribution by subtracting the effect of the method resolution. Since the uncertainty of the method is not a perfect Gaussian distribution one can't simply calculate this with

$$\sigma_{\text{true}} = \sqrt{\sigma_{\text{measured}}^2 - \sigma_{\text{method}}^2}, \qquad \text{(C1)}$$

because there is no simple single value for σ_{method} for a distribution of arbitrary shape. To account for this, a bootstrapping procedure is applied, where the uncertainty of the method is repeatedly randomly sampled and subtracted in quadrature from the total measured width of the AERA $X_{\max}$ distribution. Assuming that the spread in the AERA $X_{\max}$ distribution due to the method resolution and the true spread are uncorrelated, the distribution of the average true spread (i.e., the intrinsic spread in $X_{\max}$ due to shower-to-shower fluctuations) is estimated by

$$\sigma(X_{\max}) \equiv B_N \left(\sqrt{\text{Var}\left(\varphi_{75}\left(X_{\max}\right)\right) - \varphi_{75|1}\left(\left(\delta_{X_{\max}}\right)^2\right)} \right). \qquad \text{(C2)}$$

Note that this equation still closely mirrors Eq. C1, but with some extra steps. $B_N(x)$ we define as the distribution given by performing N bootstrapping iterations on the argument x, $\varphi_{75}(y)$ is defined as the function that samples 75% of a data series y at random for the bootstrapping of B_N, and $\varphi_{75|1}(y)$ the function that selects one value at random from $\varphi_{75}(y)$ and returns δ_y, the uncertainty on y. The first term in the square root then represents the width of the AERA $X_{\max}$ distribution of the showers and the second term is the $X_{\max}$ uncertainty estimation of the method. The number of iterations N for the bootstrapping is set at 10000 to sample the whole distribution sufficiently.

The mean and width of the $\sigma(X_{\max})$ distribution B_N can now be calculated, but also this distribution is not necessarily a Gaussian distribution. We take the mean and the quantile region equivalent to the probability contained in a 1σ standard deviation of a Gaussian (i.e., the region between the 15.87% and 84.13% quantiles) will be quoted as the mean and (asymmetric) uncertainty on $\sigma(X_{\max})$, respectively.

Appendix D: Tabulated $X_{\max}$ Moments

Table IV lists the values of the two central moments of the $X_{\max}$ distribution and their uncertainties for six energy bins.

[1] A. Coleman et al., arXiv:2205.05845, (2022).

[2] H. Falcke et al. (LOPES Collaboration), Nature **435**, 313–316 (2005).

TABLE III. Table of possible residual biases [Eq. (B2)] for geometry dependent parameters. Values are shown for each energy bin. The two right-most columns show the combined upper and lower limits by taking the extrema of the 4 parameters [Eq. (B4)]. These values are also shown in Fig. 9.

lg(E[eV]) range	$\cos(\theta)$ [g cm^{-2}]	α [g cm^{-2}]	core x [g cm^{-2}]	core y [g cm^{-2}]	Lower limit [g cm^{-2}]	Upper limit [g cm^{-2}]
[17.50, 17.65)	4.4	−3.3	0.9	−3.3	−3.3	4.4
[17.65, 17.80)	5.6	−3.9	1.2	−3.0	−3.9	5.6
[17.80, 17.95)	4.9	−4.3	2.3	−3.7	−4.3	4.9
[17.95, 18.10)	6.6	−5.9	2.8	−4.0	−5.9	6.6
[18.10, 18.25)	4.7	−6.7	2.9	−4.3	−6.7	4.7
[18.25, ∞)	5.3	−5.9	3.8	−1.0	−5.9	5.3

TABLE IV. Table of the two moments of the $X_{\max}$ distribution for the six energy bins. Also listed are the ranges and mean energies for each energy bin and the number of showers in each bin. The two $X_{\max}$ moments are listed together with, in order, their 1σ statistical and systematic uncertainties as shown in Fig. 15.

lg(E[eV]) range	$\langle$lg(E[eV])$\rangle$	N	$\langle X_{\max} \rangle \pm$ stat. $\pm$ syst. [g cm^{-2}]		$\sigma(X_{\max}) \pm$ stat. $\pm$ syst. [g cm^{-2}]	
[17.50, 17.65)	17.6	167	700.7 ±7.2	$^{+11.7}_{-19.0}$	67.1 $^{+12.8}_{-12.8}$	$^{+18.0}_{-0.4}$
[17.65, 17.80)	17.7	150	709.7 ±6.3	$^{+11.4}_{-12.5}$	55.2 $^{+9.3}_{-8.9}$	$^{+14.8}_{-0.3}$
[17.80, 17.95)	17.9	127	706.2 ±7.6	$^{+9.9}_{-10.3}$	64.9 $^{+10.8}_{-10.1}$	$^{+9.2}_{-0.7}$
[17.95, 18.10)	18.0	74	720.7 ±8.2	$^{+10.2}_{-10.5}$	52.7 $^{+9.5}_{-8.6}$	$^{+7.7}_{-0.6}$
[18.10, 18.25)	18.2	43	730.3 ±12.7	$^{+8.3}_{-11.6}$	68.3 $^{+11.9}_{-11.6}$	$^{+10.4}_{-0.3}$
[18.25, ∞)	18.4	33	771.1 ±17.9	$^{+10.1}_{-11.4}$	78.3 $^{+15.9}_{-16.0}$	$^{+9.3}_{-0.3}$

[3] O. Scholten, K. Werner, F. Rusydi Astropart. Phys. **29**, 94–103 (2008).

[4] D. Ardouin *et al.*, *Astropart. Phys.* **31**, 192–200 (2009).

[5] J. Alvarez-Muniz, W. R. Carvalho, Jr., E. Zas, Astropart. Phys. **35**, 325–341 (2012).

[6] T. Huege, M. Ludwig, C. W. James, AIP Conf. Proc. **1535**, 128 (2013).

[7] A. Nelles *et al.*, JCAP **05**, 018 (2015).

[8] A. Aab *et al.*, Phys. Rev. Lett. **116**, 241101 (2016).

[9] T. Huege, Phys. Rept. 620, 1–52 (2016).

[10] F. G. Schröder *et al.*, Bull. Am. Astron. Soc. 51, 131 (2019).

[11] W. D. Apel *et al.* (LOPES Collaboration), Phys. Rev. D **90**,062001 (2014).

[12] P. A. Bezyazeekov *et al.* (Tunka-Rex Collaboration), J. Cosmol. Astropart. P. **01**, 052 (2016).

[13] I. Petrov and S. Knurenko, in *Proceedings of the 36th International Cosmic Ray Conference*, **PoS(ICRC2019)385** (2020).

[14] A. Nelles *et al.*,Astropart. Phys. **60**, 13-24 (2015).

[15] C. Glaser *et al.*, Astropart. Phys. **104**, 64-77 (2019).

[16] S. Jansen, Ph.D. thesis, Radboud University, 2016.

[17] F. Canfora, Ph.D. thesis, Radboud University, 2021.

[18] W. D. Apel *et al.* (LOPES Collaboration), J. Cosmol. Astropart. P. **09**, 025 (2014).

[19] S. Buitink *et al.*, Phys. Rev. D **90**, 082003 (2014).

[20] S. Buitink *et al.*, Nature **531**, 70 (2016).

[21] A. Abdul Halim *et al.* (Pierre Auger Collaboration), (in press). Demonstrating Agreement between Radio and Fluorescence Measurements of the Depth of Maximum of Extensive Air Showers at the Pierre Auger Observatory. Phys. Rev. Lett.

[22] A. Aab *et al.* (Pierre Auger Collaboration), *Nucl. Instrum. Meth. A* **798**, 172–213 (2015).

[23] P. Abreu *et al.* (Pierre Auger Collaboration), J. Instrum. **7**, P10011 (2012).

[24] P. Abreu *et al.* (Pierre Auger Collaboration), Eur. Phys. J. C **81**, 966 (2021).

[25] D. Ravignani *et al.* (Pierre Auger Collaboration), in *Proceedings of the 33rd International Cosmic Ray Conference*, 0693 (2013).

[26] A. Aab *et al.* (Pierre Auger Collaboration), JCAP **08**, 019 (2014).

[27] A. Aab *et al.* (Pierre Auger Collaboration), JCAP **10**, 026 (2018).

[28] A. Aab *et al.* (Pierre Auger Collaboration), J. Instrum. **15**, P10021 (2020).

[29] P. Abreu *et al.* (Pierre Auger Collaboration), Eur. Phys. J. Plus **127**, 87 (2012).

[30] D. Heck *et al.*, FZKA Tech. Umw. Wis. B **6019**, (1998).

[31] S. Ostapchenko, Nucl. Phys. B Proc. Suppl. **151**, 143 (2006).

[32] P. Mitra *et al.*, Astropart. Phys. **123**, 102470 (2020).

[33] P. Abreu *et al.*, Astropart. Phys. **35**, 591 (2012).

[34] C. C. Finlay *et al.*, Geophysical Journal International **183**, 1216-1230 (2010).

[35] M. De Domenico *et al.*, JCAP **07**, 050 (2013).

[36] P. A. Bezyazeekov *et al.* (Tunka-Rex Collaboration), Phys. Rev. D **97**, 122004 (2018).

[37] P. Abreu *et al.* (Pierre Auger Collaboration), Nucl. Instrum. Meth. A **635**, 92–102 (2011).

[38] P. Virtanen *et al.*, Nature Meth. **17**, 261 (2020).

[39] B. Pont, Ph.D. thesis, Radboud University, 2021.

[40] J. Bellido *et al.* (Pierre Auger Collaboration), in *Proceedings of the 35th International Cosmic Ray Conference*,

PoS(ICRC2017)506 (2017).

[41] S. Petrera, personal communication (October 30, 2020).

[42] M. de Domenico *et al.*, J. Cosmol. Astropart. P. **07**, 050 (2013).

[43] P. Mitra *et al.*, Astropart. Phys. **123**, 102470 (2020).

[44] B. R. Dawson *et al.* (Pierre Auger Collaboration), in *Proceedings of the 36th International Cosmic Ray Conference*, **PoS(ICRC2019)231** (2020).

[45] C. Todero Peixoto *et al.* (Pierre Auger Collaboration), in *Proceedings of the 36th International Cosmic Ray Conference*, **PoS(ICRC2019)440** (2020).

[46] A. Aab *et al.* (Pierre Auger Collaboration), Phys. Rev. Lett. **126**, 152002 (2021).

[47] C. W. Fabjan, F. Gianotti, Rev. Mod. Phys **75**, 1243 (2003).

[48] A. Corstanje *et al.*, Phys. Rev. D **103**, 102006 (2021).

[49] T. Pierog *et al.*, Phys. Rev. C **92**, 034906 (2015).

[50] F. Riehn *et al.*, Phys. Rev. D **102**, 063002 (2020).

[51] A. Yushkov *et al.* (Pierre Auger Collaboration), in *Proceedings of the 36th International Cosmic Ray Conference*, **PoS(ICRC2019)482** (2020).

[52] M. A. Stephens, Journal of the American Statistical Association **69**, 347, 730-737 (1974).

[53] V. de Souza *et al.* (Pierre Auger Collaboration, Telescope Array Collaboration), in *Proceedings of the 35th International Cosmic Ray Conference*, **PoS(ICRC2017)522** (2017).